THEORETICAL SPECTRA AND LIGHT CURVES OF CLOSE-IN EXTRASOLAR GIANT PLANETS AND COMPARISON WITH DATA

A. BURROWS,[1] J. BUDAJ,[1,2] AND I. HUBENY[1]

ABSTRACT

We present theoretical atmosphere, spectral, and light-curve models for extrasolar giant planets (EGPs) undergoing strong irradiation for which *Spitzer* planet/star contrast ratios or light curves have been published (circa 2007 June). These include HD 209458b, HD 189733b, TrES-1, HD 149026b, HD 179949b, and υ And b. By comparing models with data, we find that a number of EGP atmospheres experience thermal inversions and have stratospheres. This is particularly true for HD 209458b, HD 149026b, and υ And b. This finding translates into qualitative changes in the planet/star contrast ratios at secondary eclipse and in close-in EGP orbital light curves. Moreover, the presence of atmospheric water in abundance is fully consistent with all the *Spitzer* data for the measured planets. For planets with stratospheres, water absorption features invert into emission features and mid-infrared fluxes can be enhanced by a factor of 2. In addition, the character of near-infrared planetary spectra can be radically altered. We derive a correlation between the importance of such stratospheres and the stellar flux on the planet, suggesting that close-in EGPs bifurcate into two groups: those with and without stratospheres. From the finding that TrES-1 shows no signs of a stratosphere, while HD 209458b does, we estimate the magnitude of this stellar flux breakpoint. We find that the heat redistribution parameter, P_n, for the family of close-in EGPs assumes values from $\sim$0.1 to $\sim$0.4. This paper provides a broad theoretical context for the future direct characterization of EGPs in tight orbits around their illuminating stars.

Subject headings: planetary systems — planets and satellites: general — stars: individual (HD 209458, HD 189733, TrES-1, HD 149026, υ Andromedae, HD 179949)

Online material: color figures

1. INTRODUCTION

To date, more than 250 extrasolar planets have been discovered and more than 29 of them are transiting their primary star.[3] One transiting planet is a "Neptune" (GJ 436b), but the rest are giant planets with an impressively wide range of masses and radii that speak to the heterogeneity of the family of close-in EGPs (extrasolar giant planets). Table 1 lists these transiting EGPs and some of their relevant properties, along with many of the references to the observational and discovery papers from which these data were taken. Table 2 lists useful data for the corresponding primary stars, including their masses, luminosities, radii, and approximate ages. Both tables are organized in order of increasing planetary semimajor axis, and, considering the pace of the field, both should be considered provisional. Not shown are the eccentricities, which are generally small, but which for HAT-P-2b, GJ 436b, and XO-3b are $\sim$0.507, $\sim$0.14, and $\sim$0.22, respectively. For these three close-in EGPs, significant tidal heating, and perhaps forcing by an unseen companion, are implied.

Radial velocity measurements for a nontransiting EGP provide a lower limit to its mass, but little else. However, the transiting EGPs yield radii as well and resolve the sin *i* ambiguity to reveal the planets' masses. These data provide physical constraints with which detailed evolutionary and structural models that incorporate irradiation and migration can be tested (see, e.g., Burrows et al. 2007a; Guillot et al. 2006). Assuming superb photometric accuracy, the wavelength dependence of the transit radii can in principle provide a measure of a planet's atmospheric composition (Fortney et al. 2003). In this way, sodium has been detected in HD 209458b (Charbonneau et al. 2002) and water has been identified in both HD 189733b (Tinetti et al. 2007, but see Ehrenreich et al. 2007) and HD 209458b (Barman 2007). Moreover, high-precision optical photometry has constrained (and possibly measured) the geometric albedo of the close-in EGP HD 209458b (Rowe et al. 2006, 2007). HD 209458b's optical albedo is very low ($\sim$3.8% $\pm$ 4.5%), in keeping with the predictions of Sudarsky et al. (2000), for cases in which the alkali metals, and not clouds, dominate absorption in the atmosphere and Rayleigh scattering dominates scattering.

Nevertheless, using current technology, transit measurements have limited utility in characterizing the atmospheres and compositions of these planets. Astronomers require more direct detections of the planet's spectrum to probe its chemistry and atmospheric properties. This is in the tradition of remote sensing in the solar system and of the Earth. Until recently it had been thought that the light from an extrasolar planet had to be separated from under the glare of its parent star using high angular resolution, extremely high contrast imaging. This is still the case in the optical for the cool "wide-separation" EGPs (Burrows et al. 2004; Sudarsky et al. 2005; Burrows 2005) and terrestrial planets, for which the planet-star contrast ratio is $\sim$10^{-9} to $\sim$10^{-10}, but such performance has not yet been demonstrated.

However, for the hot close-in EGPs, the planet-star contrast ratios in the mid-infrared are much more favorable (Burrows et al. 2003, 2004), ofttimes exceeding 10^{-3}. This capability has led to a breakthrough in the study of exoplanets. With the infrared space telescope *Spitzer* (Werner & Fanson 1995), using its IRAC and MIPS cameras and the IRS spectrometer, one can now measure the summed light of the planet and the star in and out of secondary

[1] Department of Astronomy and Steward Observatory, University of Arizona, Tucson, AZ 85721; burrows@zenith.as.arizona.edu, budaj@as.arizona.edu, hubeny@aegis.as.arizona.edu.
[2] Astronomical Institute, Tatranska Lomnica, 05960 Slovak Republic.
[3] See J. Schneider, Extrasolar Planet Encyclopedia, at http://exoplanet.eu, the Geneva Search Program at http://exoplanets.eu, and the Carnegie/California compilation at http://exoplanets.org.

TABLE 1
Transiting Planet Data

Planet	a (AU)	Period (days)	M_p (M_J)	R_p (R_J)	F_p (10^9 ergs cm^{-2} s^{-1})	References
OGLE-TR-56b	0.0225	1.2119	1.29 ± 0.12	1.30 ± 0.05	5.912	1, 2, 3, 4, 5
TrES-3....................	0.0226	1.3062	1.92 ± 0.23	1.295 ± 0.081	1.567	31
OGLE-TR-113b	0.0229	1.4325	1.32 ± 0.19	1.09 ± 0.03	0.739	1, 2, 4, 6, 7, 8
CoRoT-Exo-1b...............	0.026	1.5	1.3	$1.65-1.78$	. . .	. . .
GJ 436b....................	0.0285	2.6438	0.071 ± 0.006	0.386 ± 0.016	0.044	32, 35, 36 (8 μm)
OGLE-TR-132b	0.0306	1.6899	1.14 ± 0.12	1.18 ± 0.07	3.500	26
WASP-2b....................	0.0307	2.1522	0.88 ± 0.11	1.04 ± 0.06	0.579	10, 11
HD 189733b	0.0313	2.2186	1.15 ± 0.04	1.15 ± 0.03	0.468	4, 12, 13
WASP-3b....................	0.0317	1.8463	$1.76^{+0.08}_{-0.14}$	$1.31^{+0.07}_{-0.14}$	3.520	44
TrES-2	0.0367	2.4706	$1.28^{+0.09}_{-0.04}$	$1.24^{+0.09}_{-0.06}$	1.150	14, 27
XO-2b	0.0369	2.6158	0.57 ± 0.06	$0.973^{+0.03}_{-0.008}$	0.759	29
WASP-1b....................	0.0379	2.5199	$0.79^{+0.13}_{-0.06}$	1.40 ± 0.08	2.488	10, 15, 28
HAT-P-3b	0.0389	2.8997	0.599 ± 0.026	0.89 ± 0.046	0.395	37
TrES-1	0.0393	3.0301	0.75 ± 0.07	1.08 ± 0.3	0.428	1, 2, 4, 16, 17
HAT-P-5b	0.0408	2.7885	1.06 ± 0.11	1.26 ± 0.05	1.259	41
OGLE-TR-10b	0.0416	3.1013	0.63 ± 0.14	1.26 ± 0.07	1.344	1, 2, 4, 5, 18
HD 149026b	0.042	2.8766	0.36 ± 0.03	0.73 ± 0.03	2.089	4, 19
HAT-P-4b	0.0446	3.0565	0.68 ± 0.04	1.27 ± 0.05	1.833	39
HD 209458b	0.045	3.5247	0.64 ± 0.06	1.32 ± 0.03	1.074	4, 20, 21
OGLE-TR-111b...............	0.047	4.0144	0.52 ± 0.13	1.07 ± 0.05	0.248	1, 2, 4, 22
XO-3b	0.0477	3.1914	13.21 ± 0.43	1.94 ± 0.16	4.156	33
TrES-4	0.0488	3.5539	0.84 ± 0.10	1.674 ± 0.094	2.306	38
XO-1b	0.0488	3.9415	0.90 ± 0.07	$1.18^{+0.03}_{-0.02}$	0.485	23, 24
OGLE-TR-211b	0.051	3.6772	1.03 ± 0.20	$1.36^{+0.18}_{-0.09}$	2.034	45
OGLE-TR-182b	0.051	3.9791	1.01 ± 0.15	$1.13^{+0.24}_{-0.08}$	0.755	43
HAT-P-6b	0.0526	3.8530	1.06 ± 0.12	1.33 ± 0.06	1.755	42
HAT-P-1b	0.0551	4.4653	0.53 ± 0.04	1.203 ± 0.051	0.681	25, 34
HAT-P-2b	0.0685	5.6334	8.17 ± 0.72	1.18 ± 0.16	1.326	30
HD 17156b	0.1594	21.2173	$3.11^{+0.035}_{-0.013}$	$0.964^{+0.016}_{-0.027}$	0.161	40, 46

Notes.—Data, plus representative references, for 29 of the known transiting EGPs with measured M_p and R_p. The list is in order of increasing semimajor axis. F_p is the stellar flux at the planet's substellar point, given the stellar luminosities provided in Table 2.

References.—(1) Santos et al. 2006a, (2) Santos et al. 2006b, (3) Vaccaro & Van Hamme 2005, (4) Melo et al. 2006, (5) Pont et al. 2007a, (6) Gillon et al. 2006, (7) Bouchy et al. 2004, (8) Konacki et al. 2004, (9) Moutou et al. 2004, (10) Cameron et al. 2007, (11) Charbonneau et al. 2007, (12) Bouchy et al. 2005, (13) Bakos et al. 2006, (14) O'Donovan et al. 2006, (15) Shporer et al. 2007, (16) Alonso et al. 2004, (17) Winn et al. 2007b, (18) Holman et al. 2007, (19) Sato et al. 2005, (20) Santos et al. 2004, (21) Knutson et al. 2007a, (22) Winn et al. 2007a, (23) Holman et al. 2006, (24) McCullough et al. 2006, (25) Bakos et al. 2007a, (26) Gillon et al. 2007b, (27) Sozzetti et al. 2007, (28) Stempels et al. 2007, (29) Burke et al. 2007, (30) Bakos et al. 2007b, (31) O'Donovan et al. 2007, (32) Gillon et al. 2007c, (33) Johns-Krull et al. 2007, (34) Winn et al. 2007c, (35) Gillon et al. 2007d, (36) Deming et al. 2007, (37) Torres et al. 2007, (38) Mandushev et al. 2007, (39) Kovács et al. 2007, (40) Barbieri et al. 2007, (41) Bakos et al. 2007c, (42) Noyes et al. 2008, (43) Pont et al. 2007b, (44) Pollacco et al. 2008, (45) Udalski et al. 2007, (46) Gillon et al. 2007a.

eclipse, and use the difference between them to determine the planet's spectrum at superior conjunction. Moreover, for a subset of the closest EGPs it is possible to use *Spitzer* to measure their flux variations with planetary phase between transit and secondary eclipse. Hence, for the close-in EGPs in the near- to mid-infrared, and without the need to separately image planet and star, the direct detection of planetary atmospheres via low-resolution spectroscopy and precision infrared (IR) photometry is now a reality.

The secondary eclipse fluxes have now been measured for five transiting EGPs (HD 189733b, TrES-1, HD 209458b, HD 149026b, GJ 436b), but not yet in all *Spitzer* bands. In addition, using the IRS spectrometer, spectra between ∼7.5 and ∼15 μm of two transiting EGPs at secondary eclipse have been obtained (HD 189733b [Grillmair et al. 2007] and HD 209458b [Richardson et al. 2007]). Although at very low resolution, these are the first measured spectra of any extrasolar planet. Furthermore, light curves have been measured for three EGPs (υ And b [Harrington et al. 2006 at 24 μm], HD 179949b [Cowan et al. 2007 at 8 μm], and HD 189733b [Knutson et al. 2007b at 8 μm]). Only one of these (HD 189733b) is transiting and has an absolute calibration.

For none of the latter three are there extant light-curve measurements for more than one *Spitzer* band; for some of these EGPs only upper limits in a few of the other bands have been determined. Table 3 summarizes all the direct detection data for the EGP family obtained to date (ca. 2007 June 1), along with associated references, comments, and table notes. Clearly, in the next year or two we can expect a great deal more secondary eclipse and light-curve data in the various *Spitzer* IRAC and MIPS bands. However, there has already been significant progress in measuring EGP atmospheres.

This paper is a continuation of our series of interpretative studies (e.g., Burrows et al. 2005, 2006, 2007b) of the direct measurements of close-in EGPs. Here we analyze the secondary eclipse and light-curve data summarized in Table 3 for the EGPs HD 189733b, HD 209456b, TrES-1, HD 149026b, HD 179949b, and υ And b and make theoretical predictions in support of future *Spitzer* planet measurement campaigns. Importantly, by fitting the current data, we extract physical information concerning the atmospheres, compositions, and thermal profiles of these first six objects listed in Table 3. We have explored the dependence of the spectra and light curves on the heat redistribution factor

TABLE 2
Data on Parent Stars

Star	Spectral Type	R_* $(R_\odot)$	T_{eff} (K)	log g (cgs)	[Fe/H]$_*$	M_* $(M_\odot)$	L_* $(L_\odot)$	Age (Gyr)	Distribution (pc)	References
OGLE-TR-56	G	1.32 ± 0.06	6119	4.21	0.25	1.04	2.20	$2.5^{+1.5}_{-1.0}$	1600	1, 2, 3, 4, 5
TrES-3	G3 V	0.80 ± 0.05	5650	4.60	−0.19	0.90	0.59	...	...	31
OGLE-TR-113	K	0.77 ± 0.02	4804	4.52	0.15	0.78	0.29	5.35 ± 4.65	550	1, 2, 4, 6, 7, 8
CoRoT-Exo-1	G	1.2 ± 0.2	...	...	...	...	...	...	>460	...
GJ 436........................	M2.5 V	0.44 ± 0.04	3500	4.5	0.0	0.44	0.026	>3	10.2	32, 35, 36 (8 μm)
OGLE-TR-132	F	1.34 ± 0.08	6210	4.51	0.37	1.26	2.41	1.25 ± 0.75	2200	26
WASP-2......................	K1 V	0.81 ± 0.03	5200	4.50	...	0.79	0.44	...	...	10, 11
HD 189733	K1.5	0.76 ± 0.02	5050	4.53	−0.03	0.82	0.34	5.25 ± 4.75	19.3	4, 12, 13
WASP-3......................	F7 V	$1.31^{+0.05}_{-0.12}$	6400	4.30	...	1.24	2.60	...	223	44
TrES-2	G0 V	$1.00^{+0.06}_{-0.04}$	5960	4.40	−0.15	1.08	1.14	$4.9^{+2.9}_{-2.0}$	...	14, 27
XO-2	K0 V	$0.964^{+0.02}_{-0.009}$	5400	4.62	0.45	0.98	0.76	$5.0^{+1.0}_{-0.5}$	149	29
WASP-1......................	F7 V	1.45 ± 0.03	6110	4.28	0.26	1.3	2.67	2.0 ± 1.0	...	10, 15, 28
HAT-P-3	K V	$0.824^{+0.036}_{-0.062}$	5185	4.61	0.27	0.94	0.44	$0.4^{+6.5}_{-0.3}$	140	37
TrES-1	K0 V	0.81 ± 0.02	5226	4.40	0.06	0.88	0.49	4.0 ± 2.0	143	1, 2, 4, 16, 17
HAT-P-5	G0	1.17 ± 0.05	5960	4.37	0.24	1.16	1.54	2.6 ± 1.8	340	41
OGLE-TR-10	G	1.16 ± 0.06	6075	4.54	0.28	1.02	1.65	2.0 ± 1.0	1300	1, 2, 4, 5, 18
HD 149026	G0 IV	1.45 ± 0.10	6147	4.26	0.36	1.3	2.71	2.0 ± 0.8	78.9	4, 19
HAT-P-4	G0	1.59 ± 0.07	5860	4.14	0.24	1.26	2.68	$4.2^{+2.6}_{-0.6}$	310	39
HD 209458	G0 V	1.13 ± 0.02	6117	4.48	0.02	1.10	1.60	5.5 ± 1.5	47	4, 20, 21
OGLE-TR-111..............	G/K	0.83 ± 0.03	5044	4.51	0.19	0.81	0.40	5.55 ± 4.45	1000	1, 2, 4, 22
XO-3	F6	2.13 ± 0.2	6429	3.95	−0.18	1.41	6.96	2.8 ± 0.15	...	33
TrES-4........................	F	1.74 ± 0.09	6200	4.05	0.14	1.22	4.04	4.7 ± 2.0	440	38
XO-1	G2 V	$0.93^{+0.02}_{-0.01}$	5750	4.53	0.015	1.00	0.85	4.6 ± 2.3	200	23, 24
OGLE-TR-211	F7 V	$1.64^{+0.21}_{-0.07}$	6325	4.22	0.11	1.33	3.88	...	...	45
OGLE-TR-182............	G0 V	$1.14^{+0.23}_{-0.06}$	5924	4.47	0.37	1.14	1.44	...	...	43
HAT-P-6	F8	1.46 ± 0.06	6570	4.22	−0.13	1.29	3.57	$2.3^{+0.5}_{-0.7}$	260	42
HAT-P-1	G0 V	$1.15^{+0.10}_{-0.07}$	5975	4.45	0.13	1.12	1.52	3.6 ± 1.0	139	25, 34
HAT-P-2	F8 V	1.80 ± 0.25	6290	4.22	0.12	1.35	4.58	$2.7^{+1.4}_{-0.6}$	135	30
HD 17156	G0 V	$1.354^{+0.012}_{-0.037}$	6079	4.18	0.24	1.20	2.66	5.7 ± 1.3	78.24	40, 46

Notes.—A compilation of the physical parameters derived for the parents of 29 of the known transiting EGPs. The error bars have been rounded from those found in the literature. The ages, the least well-known quantities, should be taken with caution. The stellar metallicities are given without error bars, which are assumed to be large. Due to their great distances (rightmost column), the stellar types of the OGLE objects are not well constrained.

References.—(1) Santos et al. 2006a, (2) Santos et al. 2006b, (3) Vaccaro & Van Hamme 2005, (4) Melo et al. 2006, (5) Pont et al. 2007a, (6) Gillon et al. 2006, (7) Bouchy et al. 2004, (8) Konacki et al. 2004, (9) Moutou et al. 2004, (10) Cameron et al. 2007, (11) Charbonneau et al. 2007, (12) Bouchy et al. 2005, (13) Bakos et al. 2006, (14) O'Donovan et al. 2006, (15) Shporer et al. 2007, (16) Alonso et al. 2004, (17) Winn et al. 2007b, (18) Holman et al. 2007, (19) Sato et al. 2005, (20) Santos et al. 2004, (21) Knutson et al. 2007a, (22) Winn et al. 2007a, (23) Holman et al. 2006, (24) McCullough et al. 2006, (25) Bakos et al. 2007a, (26) Gillon et al. 2007b, (27) Sozzetti et al. 2007, (28) Stempels et al. 2007, (29) Burke et al. 2007, (30) Bakos et al. 2007b, (31) O'Donovan et al. 2007, (32) Gillon et al. 2007c, (33) Johns-Krull et al. 2007, (34) Winn et al. 2007c, (35) Gillon et al. 2007d, (36) Deming et al. 2007, (37) Torres et al. 2007, (38) Mandushev et al. 2007, (39) Kovács et al. 2007, (40) Barbieri et al. 2007, (41) Bakos et al. 2007c, (42) Noyes et al. 2008, (43) Pont et al. 2007b, (44) Pollacco et al. 2008, (45) Udalski et al. 2007, (46) Gillon et al. 2007a.

P_n (Burrows et al. 2006), on atmospheric metallicity, and on the possible presence of a stratospheric absorber. The recent analysis by Burrows et al. (2007b) of the IRAC data of Knutson et al. (2008) indicates that HD 209458b boasts a thermal inversion that radically alters the *Spitzer* fluxes and their interpretation. In fact, in Burrows et al. (2007b) we speculate that thermal inversions and stratospheres may play a role in the atmospheres of many close-in EGPs and are a new feature in the study of transiting planets. A similar conclusion was reached by Fortney et al. (2006), specifically in the context of HD 149026b.

We find that we can fit all the secondary eclipse and light-curve data, except for the nightside flux of HD 189733b and its day/night contrast. While we can fit its dayside secondary eclipse flux, we suspect that HD 189733b will require a more sophisticated day/night redistribution model than we now employ (§ 2). We note that Knutson et al. (2007b) conclude that the dimmest and brightest spots on HD 189733b reside on the same hemisphere and that the dimmest spot is shifted from the antistellar point by as much as ∼30°. Our current light-curve models are symmetric about the peak.

We find that the degree of longitudinal heat redistribution (P_n) may vary from planet to planet, hinting at a variety of meteoro-logical conditions and day/night contrasts within the family of close-in EGPs. Moreover, as was also concluded in Burrows et al. (2005), we cannot obtain good fits at secondary eclipse without the presence of water in abundance in the atmospheres of these irradiated EGPs. This is particularly true for TrES-1 and HD 209458b. Although we do not dwell in this paper on metallicity, we find that the metallicity dependence of the secondary-eclipse fluxes is not strong, although it is in principle measurable, and that the metallicity dependence of the variation of the planetary flux with phase is only modest. Importantly, we also conclude that upper atmosphere absorption in the optical by an as yet unknown molecule and the concomitant thermal inversions and stratospheres provide better fits to some of the data.

In § 2 we describe our numerical techniques, the new heat re-distribution model, and how we generate stratospheres. This section is supported with Appendices A, B, C, and D, in which we provide details concerning the heat redistribution model and de-rive some analytic formulae concerning atmospheric physics with day-night coupling. In particular, in Appendix D, we address the enhancement at secondary eclipse in the integrated planetary flux at Earth over and above what would be expected if the planet emit-ted isotropically. For a radar antenna, this would be its "gain"

TABLE 3

Spectral, Photometric, and Composition Measurements of Extrasolar Giant Planets

Planet	λ μm	Telescope/ Instrument	$F_p/F_\star$ Secondary Eclipse	$\Delta F_p/F_\star$	Comments	Reference
HD 189733 b	7.5–14.7	*Spitzer* IRS	Spectrum		No H_2O?, CH_4?	Grillmair et al. (2007)[a]
	8.0	*Spitzer* IRAC4	**0.003392(55)**	**0.0012(2)**	Light curve	Knutson et al. (2007b)[b]
	16.0	*Spitzer* IRS	**0.00551(30)**		Peak-up mode	Deming et al. (2006)
	3.6	*Spitzer* IRAC1	0.02356(020)		Primary transit depth	Beaulieu et al. (2008)
	5.8	*Spitzer* IRAC3	0.02436(020)		(Tinetti et al. 2007)	Beaulieu et al. (2008)
	8.0	*Spitzer* IRAC4	0.0239(02)		(Tinetti et al. 2007)	Knutson et al. (2007b)
TrES-1	4.5	*Spitzer* IRAC2	**0.00066(13)**		H_2O identified	Charbonneau et al. (2005)
	8.0	*Spitzer* IRAC4	**0.00225(36)**		(Burrows et al. 2005)	Charbonneau et al. (2005)
HD 209458 b	Ly α	*HST* STIS			H I, $R_p = 4.3 R_J$	Vidal-Madjar et al. (2003)[c]
	0.12–0.17	*HST* STIS			C, O	Vidal-Madjar et al. (2004)[d]
	0.3–0.5	*HST* STIS			$R_P = 1.3300(6) R_J$ at Balmer cont.?	Ballester et al. (2007)[e]
	0.58–0.64	*HST* STIS			Na D (transit)	Charbonneau et al. (2002)[f]
	$\sim$0.94	*HST* STIS			H_2O identified (transit)	Barman 2007
	0.4–0.7	*MOST*	$<1.34 \times 10^{-4}$ (3 σ)		$A_g < 0.68$ (3 σ)	Rowe et al. (2006)[g]
			$<4.88 \times 10^{-5}$ (1 σ)		$A_g < 0.25$ (1 σ)	Rowe et al. (2006)
	0.4–0.7	*MOST*	$<3.9 \times 10^{-5}$ (1 σ)		$A_g \sim 4.0 \pm 4.0\%$	Rowe et al. (2007)
	2.2	IRTF SpeX	<0.0003 (1 σ)			Richardson et al. (2003)
	3.6	*Spitzer* IRAC1		<0.015 (2 σ)	Light curve	Cowan et al. (2007)
	8.0	*Spitzer* IRAC4		<0.0015 (2 σ)	Light curve	Cowan et al. (2007)
					$P_n \gtrsim 0.32$ (1 σ)	
	3.6	*Spitzer* IRAC1	**0.00094(9)**		Temperature inversion	Knutson et al. (2008)
	4.5	*Spitzer* IRAC2	**0.00213(15)**		H_2O in emission	Knutson et al. (2008)
	5.8	*Spitzer* IRAC3	**0.00301(43)**			Knutson et al. (2008)
	8.0	*Spitzer* IRAC4	**0.00240(26)**		(Burrows et al. 2007b)	Knutson et al. (2008)
	7.5–13.2	*Spitzer* IRS	Spectrum		Features at 7.78, 9.65 μm?	Richardson et al. (2007)[h]
					No H_2O, CH_4?	
	8.2–13.2	*Spitzer* IRS	Spectrum		$F_p = 0.40 \pm 0.19$ mJy at 12 μm	Swain et al. (2008)[i]
	24.0	*Spitzer* MIPS	**0.00260(46)**			Deming et al. (2005)
	24.0	*Spitzer* MIPS	**0.0033(3)(?)**			Deming (private communication)
HD 149026 b	8.0	*Spitzer* IRAC4	**0.00084(11)**			Harrington et al. (2007)
υ And b	24.0	*Spitzer* MIPS	No transit	**0.0029(7)**	Light curve	Harrington et al. (2006)
HD 179949 b	3.6	*Spitzer* IRAC1	No transit	<0.019 (2 σ)	Light curve	Cowan et al. (2007)
	8.0	*Spitzer* IRAC4	No transit	**0.00141(33)**	Light curve	Cowan et al. (2007)[j]
					$P_n \lesssim 0.30$ (1 σ)	
GJ 436b	8.0	*Spitzer* IRAC4	**0.00057(8)**			Deming et al. (2007)
						Demory et al. (2007)
51 Peg b	4.5	*Spitzer* IRAC2	No transit	<0.017 (2 σ)	Light curve	Cowan et al. (2007)
	8.0	*Spitzer* IRAC4	No transit	<0.0007 (2 σ)	Light curve	Cowan et al. (2007)
OGLE-113 b	2.2	NTT SOFI	0.0017(5) (3 σ)?			Snellen & Covino (2007)

Notes.—This table contains the following columns: the name of the planet, spectral region of the observations, the telescope with the instrument used for the observations, the planet to star flux ratio during the secondary eclipse ($F_p/F_\star$), the amplitude or peak to trough variations of the light curve ($\Delta F_p/F_\star$), brief comments, and the reference. Numbers in bold are measurements (not upper limits) at secondary eclipse or actual light-curve ($\Delta F_p/F_\star$) measurements. Models for all these data in boldface (except the 8 μm point for GJ 436b at secondary eclipse) are presented in this paper. Numbers in parentheses are errors in the last digits.

[a] Grillmair et al. (2007) argue that a flat spectrum is caused by the lack of significant water or methane absorption. However, this is not consistent with the conclusions of Tinetti et al. (2007), using the primary eclipse data of Beaulieu et al. (2008) and Knutson et al. (2007b).

[b] Knutson et al. (2007b) also derived the longitudinal dependence of the surface brightness and found a hot spot shifted by $16° \pm 6°$ east of the substellar point while the coolest region was shifted about $30°$ west of the antistellar point. They also found an indication of nonzero eccentricity with $e \cos \omega = 0.0010 \pm 0.0002$, a transit radius at 8 μm of $1.137 \pm 0.006 R_J$, a stellar radius of $0.757 \pm 0.003 R_\odot$ and an inclination of $85.61° \pm 0.04°$, where ω is the longitude of periastron.

[c] Vidal-Madjar et al. (2003) detected atomic hydrogen in the planet's atmosphere with a transit absorption depth of $15\% \pm 4\%$ (1 σ), and evaporation at the rate of $\geq 10^{10}$ g s^{-1}.

[d] Vidal-Madjar et al. (2004) detected oxygen and carbon in the planet's atmosphere.

[e] Ballester et al. (2007) claim to have identified H I absorption in the Balmer continuum, but Barman (2007) challenges this interpretation.

[f] Charbonneau et al. (2002) found that the transit depth at the Na D feature is deeper by $2.32 \pm 0.57 \times 10^{-4}$ than in the continuum, which is interpreted as a detection of Na in the planet's atmosphere.

[g] Rowe et al. (2006) established the constraints $A_g < 0.25$ (1 σ) or $A_g < 0.68$ (3 σ), but Rowe et al. (2007) constrained A_g to be below 8% to 1 σ. A_g is the geometric albedo in the optical.

[h] Richardson et al. (2007) claim to have detected a broad emission peak centered near 9.65 μm which they attribute to the emission by silicate clouds, and a narrow unidentified emission feature at 7.78 μm. They say that models with water absorption fit the data poorly. However, Burrows et al. (2007b) conclude that water is in fact seen in emission, not absorption.

[i] Swain et al. (2008) determined the planet flux at 12 μm to be 0.40 ± 0.19mJy and the normalized secondary eclipse depth to be 0.0046 ± 0.0006. They are updating their absolute calibrations.

[j] Cowan et al. (2007) constrain P_n for HD 209458b and HD 179949b to be $P_n > 0.32$ (1 σ) and $P_n < 0.30$(1 σ), respectively; P_n is the fraction of the total energy incident on the day side of the planet which is transferred to and radiated out on the night side of the planet.

factor. In § 3 we discuss the derived temperature-pressure pro-files on the day and the night sides for all six EGPs highlighted in this investigation. We show that the $\tau = \frac{2}{3}$ decoupling layers for the *Spitzer* IRAC and MIPS (24 μm) band fluxes are all above the isothermal region of an irradiated EGP's atmosphere, and hence that *Spitzer* does not probe these deeper regions. For the same reasons, we find that the presence of a thermal inversion at alti-tude and of a stratosphere in some EGP atmospheres can signifi-cantly alter these *Spitzer* fluxes and their relative strengths. In § 3 we also provide representative planet spectra to demonstrate that most of the planet's flux emerges at shorter wavelengths than are accessible to *Spitzer*, and hence that *Spitzer* probes only a small tail of the emergent flux distribution. This may be of relevance when the *James Webb Space Telescope* (*JWST*) is available to fol-low up on the *Spitzer* EGP data, and even earlier as the *JWST* exoplanet campaign is being designed.

In § 4 we present the best-fit planet-star contrast ratios at sec-ondary eclipse for four of the transiting EGPs for which these have been measured (all but GJ 436b, for which see Deming et al. 2007 and Demory et al. 2007), as well as various comparison models to gauge a few parameter dependences. Then in § 5 we match our theoretical phase light curves with the three measured light curves and derive approximate planetary parameters. The paper is brought to a close in § 6 with a synopsis of our results and a general discussion of the issues raised.

2. NUMERICAL TECHNIQUES

Our model atmospheres are computed using the updated code COOLTLUSTY, described in Sudarsky et al. (2003), Hubeny et al. (2003), and Burrows et al. (2006), which is a variant of the univer-sal spectrum/atmosphere code TLUSTY (Hubeny 1988; Hubeny & Lanz 1995). The molecular and atomic opacities are taken from Sharp & Burrows (2007), and the chemical abundances, which include condensate rainout, are derived using the thermochemical model of Burrows & Sharp (1999), updated as described in Sharp & Burrows (2007) and Burrows et al. (2001).

To handle convection, we use standard mixing-length theory, with a mixing length equal to the pressure scale height. The stel-lar irradiation boundary condition is numerically challenging and has not been done properly by some workers in the past. To ensure an accurate numerical solution with a nonzero incoming specific intensity, we use the formalism discussed in Hubeny et al. (2003). The stellar spectral models are taken from Kurucz (1994) for the six stars listed in Table 2 that are the primaries of the EGPs on which we focus in this paper. The day and night sides are ap-proached differently, using the new algorithm described in Ap-pendix A for the latter, which, quite naturally, experiences no incident flux but receives heat from the irradiated day side. An important additional feature of our new heat redistribution for-malism is the capacity to match both the entropy and the gravity at the base of both the day- and the nightside atmospheres. Since the inner convective zone, which constitutes most of the planet, is isentropic, this is the physically correct procedure. For a dayside calculation, we can assume a given interior flux effective tempera-ture, T_{int} (a standard number could be 75 K). For a given gravity and irradiation regime, this leads to an atmosphere solution on the day side. This solution incorporates an entropy in the convective zone. For the nightside atmosphere, we can adjust the nightside T_{int} until the entropy in its convective interior matches that found in the dayside convective zone. One product of this procedure is a connection between dayside and nightside T_{int} that has a bear-ing on overall planet cooling and shrinkage (Burrows et al. 2007a). However, since for a given measured planet radius, this mapping does not have a significant effect on the close-in planet's spectrum,

we do this here only approximately and leave to a later paper a general discussion of this topic.

The simple parameterization we use to simulate the effects of an extra stratospheric absorber entails placing an absorber with constant opacity, κ_e, in the optical frequency range $(\nu_0, \nu_1) = (3 \times 10^{14}$ Hz, 7×10^{14} Hz$)$ and high up at altitude, where the pres-sure is below a prescribed value, generally taken to be 0.03 bars. Hence, κ_e is the most important parameter to be adjusted. We could easily introduce a specified frequency and/or depth de-pendence, but this would add free parameters which we feel are not justified at this stage. We have also generated models in which TiO and VO are allowed to assume their chemical-equilibrium up-per atmosphere abundances (Sharp & Burrows 2007), uncorrected for the cold-trap effect (§ 6; Burrows et al. 2007b), and to gener-ate a stratosphere. These TiO/VO models produce qualitatively the same effects as do our ad hoc models. However, in this paper we prefer the flexibility of the κ_e prescription.

In Burrows et al. (2006), once the day- and nightside atmo-spheres were calculated, we used a two-dimensional (2D) radiative transfer code to determine the integrated emissions "at infinity" at a given viewing angle from the planet-star axis for the day- and nightside hemispheres. These numbers were then transformed into a light curve as a function of wavelength and planetary phase an-gle using the methods described in Sudarsky et al. (2000, 2005). However, we have found that since the detailed shape of the light curve connecting the day- and the nightside fluxes is likely to be only poorly constrained for the foreseeable future and since our model is symmetric about secondary eclipse, it is inappropriate to invest a disproportionate amount of effort in performing ex-pensive 2D transfer calculations. Rather, we invest our efforts in obtaining state-of-the-art day- and nightside fluxes at secondary and primary eclipse and then connecting them with a simple, al-though well-motivated, curve. Therefore, our light-curve model is

$$C = \frac{D+N}{2} + \frac{D-N}{2} \cos \alpha \sin i, \qquad (1)$$

where C is the planet/star flux ratio, D is the dayside flux (see Fig. 4), N is the nightside flux, α is the phase angle, and i is the inclination angle ($\sim 90°$ if in transit). This is the form adopted in Cowan et al. (2007). Using this simpler approach does not entail implying more precision than is warranted at this preliminary stage of inquiry.

We have revisited the question of what type of averaging of the incoming radiation from the star over the surface of the planet is best suited to describe the planetary spectrum close to the sec-ondary eclipse. We had demonstrated earlier (Sudarsky et al. 2005) that detailed 2D phase-dependent spectra averaged over the phase are equal, within a few percent, to the spectrum computed for a representative model atmosphere constructed on the assumption that the incoming flux is distributed evenly over the surface of the day side. In the usual terminology, this corresponds to the flux dis-tribution factor $f = \frac{1}{2}$ (Burrows et al. 2000).[4]

However, the spectrum of a planet observed close to the sec-ondary eclipse should be biased toward a higher flux than that obtained using the $f = \frac{1}{2}$ model. This is because the hottest part of the planet, the substellar point, is seen as emerging from the planet perpendicularly to the surface, thus showing the lowest amount of limb darkening. Therefore, the contribution of the hottest part of

---

[4] We allow the planet to be irradiated by the full flux received from the star; it is only deeper in the atmosphere where the energy is transported to the night side. See Appendix A.

the planet is maximized. To study this effect, we have computed a series of model atmospheres corresponding to a number of distances from the substellar point and have integrated the individual contributions to get the flux received by an external observer at a phase close to superior conjunction. It turns out that the flux is very close to that computed for $f = \frac{2}{3}$, which is the value we subsequently use in all simulations presented here. There is a simple analytic argument why f should be approximately equal to $\frac{2}{3}$, which we present in Appendix D.

The formalism for D and N is the best we have fielded to date. Nevertheless, a three-dimensional (3D) general circulation model (GCM) that incorporates state-of-the-art opacities, compositions, and radiative transfer will be needed to properly address day-night heat redistribution, the vortical and zonal mass motions, and the positions of the hot and cold spots. Such a model is not yet within reach, although there have been preliminary attempts to treat the physics involved (Showman & Guillot 2002; Cho et al. 2003; Menou et al. 2003; Williams et al. 2006; Cooper & Showman 2005; Lunine & Lorenz 2002). The proper GCM physics remains the major uncertainty in current planetary secondary eclipse and light-curve modeling.

3. TEMPERATURE-PRESSURE PROFILES

We have used the techniques outlined in § 2 and in Appendix A and the data in Tables 1 and 2 to create models of six of the close-in EGPs in Table 3 for which there are *Spitzer* secondary eclipse or phase light-curve data. These planets are HD 209458b, HD 189733b, TrES-1, HD 179949b, HD 149026b, and υ And b. The product of our investigation is an extensive collection of atmosphere models, with associated spectra, for many combinations of planet, P_n, metallicity, and values of P_0/P_1 (Appendix A). We have, however, settled on presenting in this paper only the central and essential results for each planet, in the knowledge that the data are not yet exquisitely constraining.

We focus on models with solar metallicity (Asplund et al. 2006) opacities, $(P_0, P_1) = (0.05, 0.5)$ bars, and an interior flux T_{int} of 75 K. These are our baseline model parameters. For a given measured planet radius, the dependence of the models on T_{int} is extremely weak. We find that the specific pressure range (P_0, P_1) in which most of the heat carried from the day side to the night side is conveyed plays a role in the planet-star flux ratios, but a subtle one. Therefore, in lieu of a comprehensive, and credible, 3D climate model, we prefer not to claim too much concerning the details of atmospheric circulation and heat redistribution. We also explore the effects of a stratospheric absorber with an optical opacity of κ_e (see also Burrows et al. 2007b). We find that such models will be most important for close-in EGPs with the greatest stellar insolation, and guided by this principle, which is particularly relevant for HD 209458b, HD 149026b, and υ And b, we explore the consequences.

Figure 1 portrays in six panels the temperature-pressure (T/P) profiles of a representative collection of dayside and nightside models of the six close-in EGPs of this study. For the day side, the different curves correspond to different values of P_n from 0.0 (no redistribution) to 0.5 (full redistribution) and to models with and without stratospheric absorbers. For the night side, P_n ranges from 0.1 to 0.5. For all models, the radiative-convective boundaries are identified and are quite deep (*far right of each panel*). When $\kappa_e \neq 0$, the T/P profiles show distinct thermal inversions.

There are quite a few generic features in evidence on these panels. The first is that the atmospheres are never isothermal. Since the opacities in the optical, where most of the stellar irradiation occurs, and in the infrared, where most of the reradiation occurs,

are very different, a quasi-isothermal inner region interior to ~1 bar is always bounded by an outer region in which the temperature decreases (Hubeny et al. 2003). As Figure 1 indicates, the magnitude of the temperature decrease from the plateau to the ~10^{-5} bar level for dayside models without stratospheres is ~1000 K. With a stratosphere, the outward increase from a pressure of ~0.1 bars can be correspondingly large. For our nightside models, the monotonic decrease is ~500–1000 K. Models with temperature inversions due to a strong absorber at altitude clearly stand out in the panels of Figure 1 and may result from the presence of a trace species, TiO/VO, or a nonequilibrium species (Burrows et al. 2007b). The possible effect of such upper atmosphere absorbers on the T/P profiles and the resultant dayside spectra are exciting new features of the emerging theory of irradiated EGPs.

The discussion above is made more germane when we note that the decoupling surfaces for the IRAC and MIPS (24 μm) channels, the effective photospheres where $\tau_\lambda \sim \frac{2}{3}$, are all in the outer zone. Figure 1 indicates their positions for the dayside $P_n = 0.3$ model of TrES-1. They are at similar pressures for all other models. The photospheres for shorter wavelengths not accessible to *Spitzer* are deeper in. Figure 2 illustrates this fact by showing these "formation," "brightness," or photospheric temperatures as a function of wavelength for three models of TrES-1 with different values of P_n, and for both the day side and night side. The approximate wavelength intervals of the *Spitzer* bands are superposed. Although the IRAC 1 flux can decouple at interesting depths, the photospheres for the Y, J, H, and K bands are generally deeper. The photospheres in the far-IR beyond ~10 μm are high up at altitude, where, as mentioned above, *Spitzer* photometry does not probe the isothermal region that is so characteristic of theoretical close-in EGP atmospheres. Moreover, since the *Spitzer* observations probe the outer regions of the atmosphere most affected by stellar irradiation, which can also have inversions, the treatment of the outer boundary condition due to incoming stellar flux must be accurate. Slight errors or uncertainties in the outer boundary condition of the transfer solution, or in the upper atmosphere opacities, can translate into significant errors in the predicted *Spitzer* fluxes. This is particularly true longward of ~10 μm. As a result, measured fluxes in both the near-IR and mid-IR are useful diagnostics of upper atmosphere absorbers and thermal inversions (Hubeny et al. 2003; Burrows et al. 2006, 2007b; Knutson et al. 2008). All these caveats and points must be borne in mind when interpreting the *Spitzer* EGP data.

As a prelude to our discussions in §§ 4 and 5 of the *Spitzer* planet-star flux ratios at secondary eclipse and during an orbital traverse, and to emphasize the fact that *Spitzer* does not comprehensively probe the irradiated planet's atmosphere, we plot in Figure 3 theoretical dayside spectra [λF_λ vs. $\log_{10}(\lambda)$] for three models of TrES-1 at zero phase angle (superior conjunction). Superposed on the plot are the positions of the near-IR, IRAC, and MIPS bands. Such a figure allows one to determine at a glance the wavelengths at which most of the flux is radiated (at least, theoretically). As Figure 3 suggests, most of the planet's flux emerges in the near-IR, not in the IRAC or MIPS channels. In fact, depending on the planet, no more than 1/5 to 1/3 of the planet's flux comes out longward of ~3.6 μm (IRAC 1), while no more than 1/20 to 1/10 emerges longward of ~6.5 μm, the "left" edge of the IRAC 4 channel. Since much of the best EGP data have been derived in IRAC channel 4, one must acknowledge that they may represent very little of the total planetary emissions.

Finally, we call the reader's attention to the slight bumps (on the night side) and depressions (on the day side) between 0.05
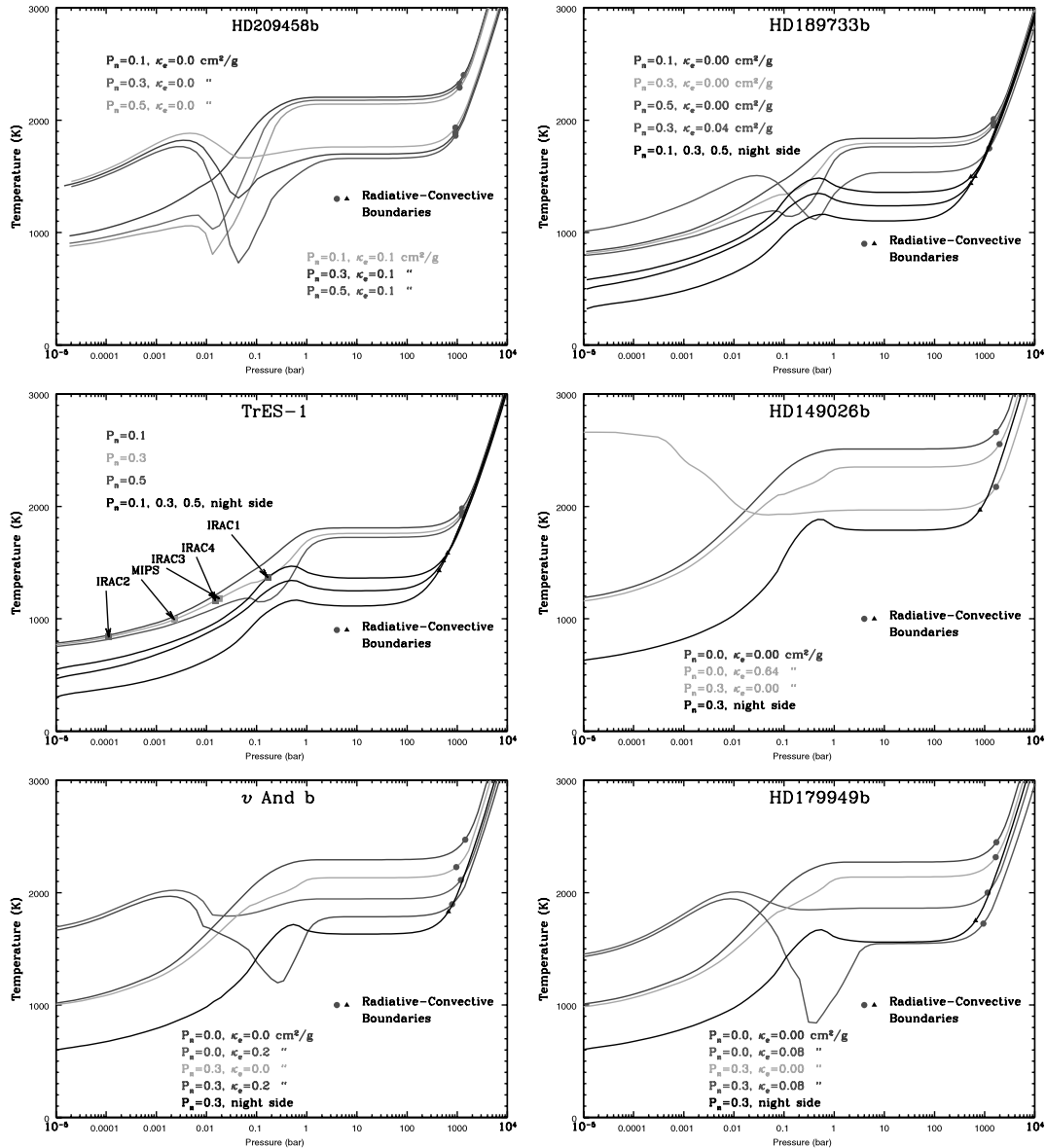
Fig. 1.—Temperature-pressure profiles for the six close-in planets studied in this paper. Dayside profiles incorporate the external substellar irradiation/flux given in Table 1 and an internal flux for the planet corresponding to the temperature of 75 K at the lower boundary. A sink of energy corresponding to the particular value of P_n was introduced between pressures of 0.05 and 0.5 bars. The night side is calculated without irradiation, assuming an energy source corresponding to the same value of P_n at the same pressures employed for the dayside sink. Entropies at the bases of the convection zones on the day and night sides were approximately matched by adjusting the internal planetary flux at the bottom of the nightside model at the same gravity. Models with an extra upper-atmosphere absorber in the optical are included for HD 209458b, HD 189733b, HD 149026b, υ And b, and HD 179949b. See text in § 3 for a discussion of these panels. [*See the electronic edition of the Journal for a color version of this figure.*]

and 1.0 bars in the T/P profiles depicted in Figure 1. This region is near where we imposed heat redistribution using the formalism described in Appendix A. The actual shapes of these profiles are determined by this mathematical procedure, and other algorithms will produce different local thermal profiles. Note that with this formalism it is possible at the higher P_n-values (≥ 0.35) for the night side to be hotter than the day side at the same pressure levels in the redistribution region. While this may seem at odds with thermodynamics, the essential point is that energy is conserved and is redistributed at optical depths that are not either too low or too high. If the former, the absorbed stellar heat would be reradiated before it could be carried to the night side. If the latter, then the stellar radiation could not penetrate to the conveyor belt. For our default choice of P_0 and P_1, τ_{Ross} is generally between

~ 0.3 and ~ 6. These depths are not unreasonable, but our redistribution algorithm is clearly only a stopgap until a better GCM can be developed and justified.

4. PLANET-STAR FLUX RATIOS: COMPARISON WITH DATA

In this section we discuss and then model fits for each transiting EGP at secondary eclipse. However, first we present our results collectively and in summary fashion. Figure 4, in four panels, portrays for the four transiting EGPs the correspondence between the secondary eclipse data and representative models of the planet-star flux ratio as a function of wavelength from 1.5 to 30 μm. This figure summarizes our major results. The models are for values of P_n of 0.1, 0.3, and 0.5 and various values of κ_e. The
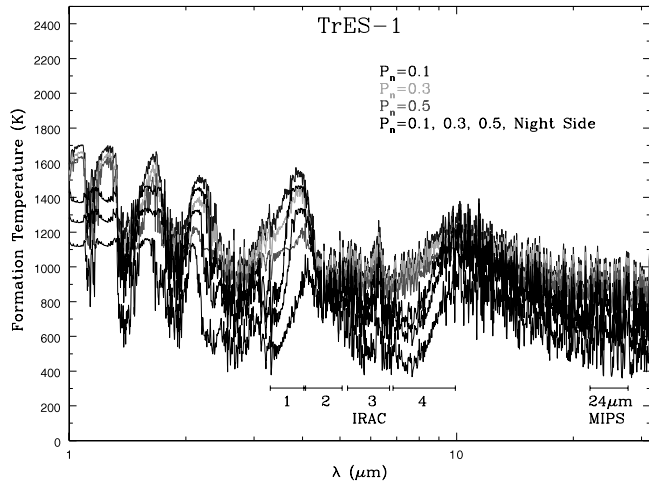
FIG. 2.—"Brightness" or "formation" temperature spectra on the day side for three models ($P_n = 0.1$, 0.3, and 0.5) of TrES-1. The formation temperature at the particular wavelength is the temperature where the optical depth at this wavelength reaches $\frac{2}{3}$. See text for a discussion. [*See the electronic edition of the Journal for a color version of this figure.*]
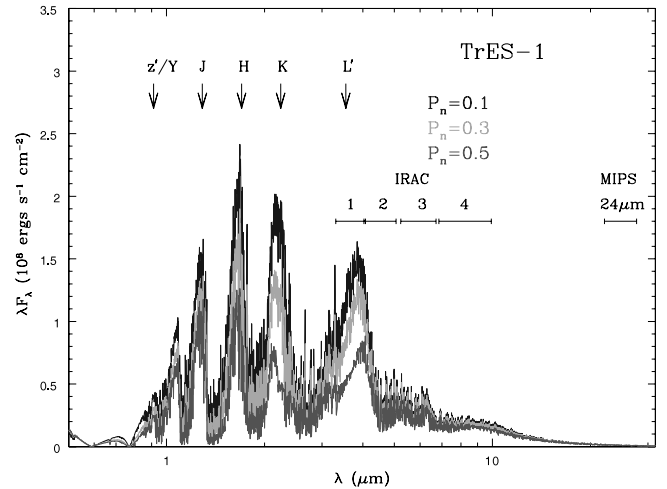

FIG. 3.—Spectral energy distribution (SED) [λF_λ vs. $\log_{10}(\lambda)$] for the day side of TrES-1 for three values of the day-night heat redistribution parameter P_n. Notice that observations in IRAC and MIPS bands cover only a small fraction of the SED of the planet. [*See the electronic edition of the Journal for a color version of this figure.*]

data include 1 σ error bars and can be found in Table 3. As Figure 4 indicates, we can fit all the published data. The P_n dependence for both stratospheric models and models without inversions is strongest in the K band and in IRAC 1. In fact, in the near-IR, models with inversions depend very strongly on P_n. Figure 5, for HD 209458b in the near-IR, indicates this most clearly. This finding implies that measurements at these shorter IR wavelengths are good diagnostics of P_n, particularly if inversions are present.

Importantly, including a nonzero κ_e and generating a stratosphere results in a pronounced enhancement longward of IRAC 1, particularly in IRAC 2 and 3, but also at MIPS 24 μm and at the 16 μm peak-up point of *Spitzer* IRS. Hence, fluxes at the longer IR wavelengths might be good diagnostics of thermal inversions. The models in Figure 4 for HD 209458b and HD 149026b demonstrate this feature best.

No attempt has been made to achieve refined fits, but the correspondence between theory and measurement, while not perfect, is rather good for all the planets. Moreover, different EGPs seem to call for different values of P_n and κ_e, and hence possibly different climates, degrees of heat redistribution, compositions, and upper atmospheric physics. The light-curve analyses in § 5 suggest the same result. A goal is to relate these measured differences with the physical properties of the star and planet, and these infrared secondary eclipse data allow us to begin this program in earnest.

We note that comparisons between model and data must actually be made after the band-averaged flux-density ratios of the detected electrons are calculated. Performing this calculation slightly mutes the predicted variation from channel to channel in the IRAC regime. This is particularly true when comparing IRAC 1 and IRAC 2, even if a pronounced spectral bump at and near ~3.6 μm obtains, as it does for models with modest or no thermal inversion. However, to avoid the resultant clutter and confusion, we do not plot these bandpass-averaged predictions on Figures 4 and 5. We now turn to case-by-case discussions of the secondary eclipse measurements and models.

4.1. *HD 209458b*

The first transiting EGP discovered was HD 209458b (Henry et al. 2000; Charbonneau et al. 2000), and it has since been intensively studied. The direct-detection data of relevance to this paper are summarized in Table 3. The most relevant data are the geometric albedo constraints in the optical from the Molonglo Observatory Synthesis Telescope (MOST; Rowe et al. 2006, 2007), a K-band upper limit using IRTF SpeX from Richardson et al. (2003), a MIPS 24 μm photometric point from Deming et al. (2005; and its possible update), a low-resolution *Spitzer* IRS spectrum from Richardson et al. (2007), and, importantly, photometric points in IRAC channels 1 through 4 from Knutson et al. (2008). These data collectively provide useful information on the atmosphere of HD 209458b.

Motivated by the recent data of Knutson et al. (2008), Burrows et al. (2007b) provide partial theoretical explanations for HD 209458b's atmosphere. Much of the discussion in the current paper concerning HD 209458b is taken from Burrows et al. (2007b), so we refer the reader to both the Burrows et al. (2007b) and Knutson et al. (2008) papers for details. However, here we expand on the discussion in those works, for which it is necessary to put the HD 209458b findings in the broader context of the EGPs listed in Table 3. The major conclusion of Burrows et al. (2007b) is that the atmosphere of HD 209458b has a thermal inversion and a stratosphere, created by the absorption of optical stellar flux by a strong absorber at altitude, the origin of which is currently unknown. This converts absorption features into emission features, while still being consistent with the presence of water in abundance.

All relevant data, save the albedo constraint in the optical, are displayed in the top left panel of Figure 4. Figure 5 includes the Knutson et al. (2008) IRAC 1 point and the Richardson et al. (2003) upper limit in K and focuses on the near-IR. Also provided on both figures are models for $P_n = 0.1$, 0.3, and 0.5, without and with an extra stratospheric absorber. The latter is implemented using the formalism in outlined in § 2 and a κ_e of 0.1 cm^2 g^{-1}.

Figure 4 shows that the low upper limit of Richardson et al. (2003) in the K band that was problematic in the old default theory (Burrows et al. 2005, 2006; Fortney et al. 2005; Barman et al. 2005; Seager et al. 2005) is consistent with the models with an extra upper atmosphere absorber in the optical, particularly for higher values of P_n. This is more clearly seen in Figure 5. Moreover, the theoretical peak near the IRAC 1 channel (~3.6 μm) in the old model without an inversion is reversed with the extra absorber into a deficit that fits the Knutson et al. (2008) point. The

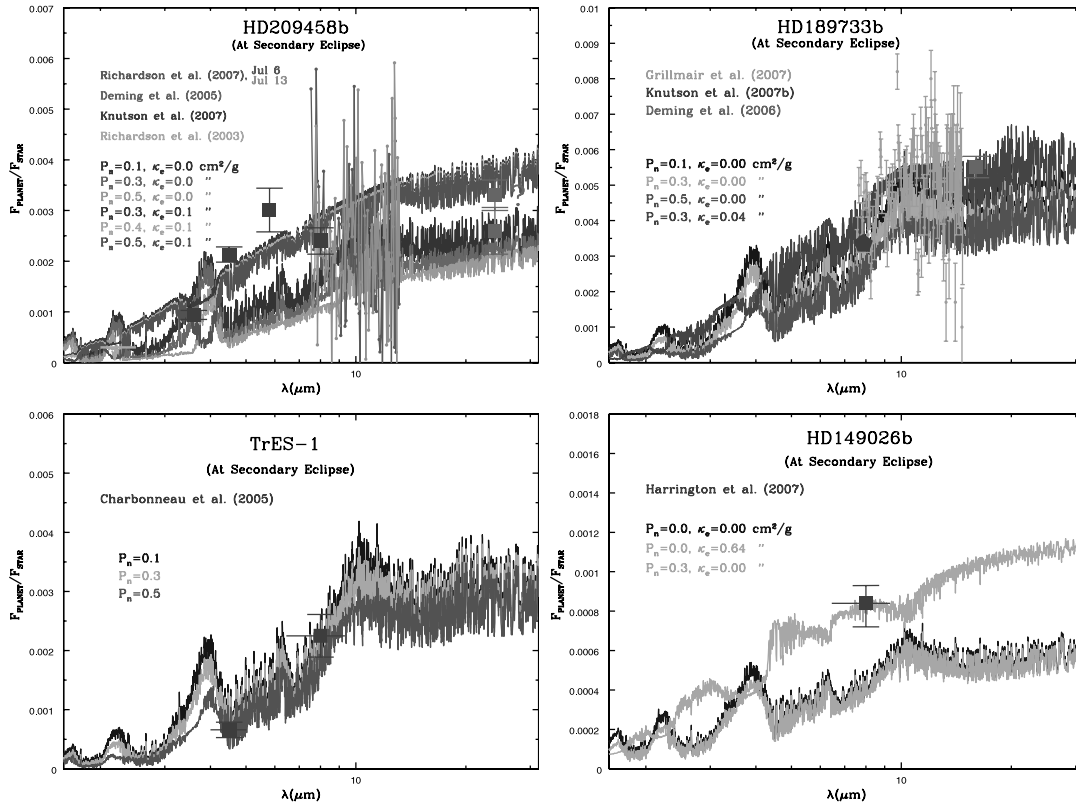Fig. 4.—Planet/star flux ratios vs. wavelength from ~1.5 to 30 μm for various models of four transiting EGPs measured by *Spitzer* at secondary eclipse. Notice the different scales employed in each panel. Models for different values of P_n (Appendix A) and κ_e are provided where appropriate and the data from Table 3 for each planet are superposed. The plot legends indicate the color schemes used for the different EGPs. On the top left panel (HD 209458b), models with the lighter gray shade(s) are for the higher value(s) of P_n. Notice also that two different values for the flux at 24 μm (*green*) are shown on this same panel. The one with the question mark is a tentative update to the Deming et al. (2005) 24 μm measurement, kindly provided by D. Deming (private communication). If the flux at 24 μm is indeed ~0.0033 ± 0.0003, then our model(s) with inversions provide the best fit at that wavelength as well. Note that the comparison between model and data should be made after the band-averaged flux-density ratios of the detected electrons are calculated. This not only incorporates the significant widths of the *Spitzer* bandpasses, but the fact that one should compare photon counts (or detected electrons), and not monochromatic fluxes. The result is that the theoretical IRAC predictions do not actually vary on the figures as much as do the plotted spectra and that the predicted contrasts, for instance between IRAC 1 and IRAC 2, are more muted, even when the pronounced bump at and near ~3.6 μm obtains. However, to avoid the resultant clutter, we do not put these bandpass predictions on these spectral plots. See text for a discussion of each irradiated planet and the inferences drawn. [*See the electronic edition of the Journal for a color version of this figure.*]
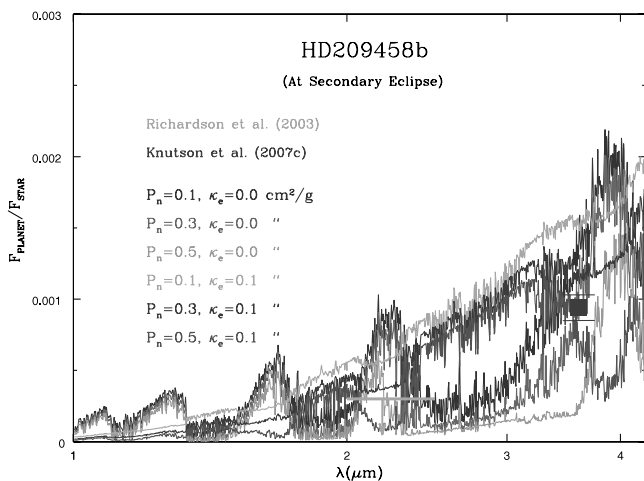
Fig. 5.—Same as Fig. 4, but for various models of HD 209458b between 1 and 4 μm. The dependence on both P_n and the presence and strength of a thermal inversion is greatest in this wavelength region. Note that a thermal inversion flips what would be water absorption features into emission features, altering the interpretation of any data in this spectral region significantly. Superposed is the Knutson et al. (2008) data point for IRAC 1 and the Richardson et al. (2003) upper limit near 2.2 μm. See text for a discussion. [*See the electronic edition of the Journal for a color version of this figure.*]

theory without an extra absorber at altitude predicts that the planet-star flux ratio in the IRAC 2 channel should be lower than the corresponding ratio at IRAC 1. However, with the extra absorber the relative strengths in these bands are reversed, as are the Knutson et al. (2008) points. This reversal is a direct signature of a thermal inversion in the low-pressure regions of the atmosphere and an indirect signature of the placement of the heat redistribution band (see Appendix A). The top left panel of Figure 1 depicts the corresponding temperature-pressure profiles and the thermal inversion at low pressures introduced by the presence of an extra absorber in the optical that is indicated by the data.

As Figure 4 also demonstrates, there is a significant difference in the IRAC planet-star flux ratios between the old default model without an inversion and the new models with a stratospheric absorber, and it shows that the models with a stratosphere fit the IRAC channel 1, 2, and 4 flux points much better. However, the height of the IRAC 3 point near 5.8 μm is not easily fit while simultaneously maintaining the good fits at the other IRAC wavelengths and consistency with the *K*-band limit. Theoretically, the positions of the IRAC 3 and IRAC 4 photospheres should be close to one another, so this discrepancy is surprising. Nevertheless, the IRAC 2, 3, and 4 data together constitute a peak, whereas in the default theory an absorption trough was expected.

The 24 μm MIPS point obtained by Deming et al. (2005) is lower than the prediction of our best-fit model. However, the flux at this point is being reevaluated and may be closer to $\sim$0.0033 $\pm$ 0.0003 (D. Deming, private communication). If the new number supersedes the old published value, then our best-fit model(s) with inversions fit at this mid-IR point as well (Fig. 4). Higher planetary fluxes longward of $\sim$10 μm are generic features of stratospheric inversions.

The 1 σ optical albedo limit from Rowe et al. (2007) is a very low 8.0%. For comparison, the geometric albedos of Jupiter and Saturn are $\sim$40%. However, such a low number was predicted due to the prominence in the optical of broadband absorptions by the alkali metals sodium and potassium in the hot atmospheres of irradiated EGPs (Sudarsky et al. 2000, their "Class IV"). The associated planet-star flux ratios are $\sim 10^{-5}$ to 10^{-6}. This low albedo is consistent with the identification of sodium in the atmosphere of HD 209458b using *HST* STIS transit spectroscopy (Charbonneau et al. 2002). Both these data sets suggest that any clouds that might reside in the atmosphere of HD 209458b are thin. A thick cloud layer would reflect light efficiently, leading to a high albedo. If the extra stratospheric absorber is in the gas phase, and there is no cloud, then our new thermal inversion models are easily consistent with the low albedo derived by Rowe et al. (2006, 2007). If the extra absorber is a cloud, the cloud particles must have a low scattering albedo and cannot be very reflecting. This rules out pure forsterite, enstatite, and iron clouds.

The IRS data are noisy, but their flattish shape is consistent with our model(s) with thermal inversions and a stratosphere. Richardson et al. (2007) suggest that there is evidence in the IRS data for two spectral features: one near 7.78 μm and one near 9.67 μm. However, we think the data are too noisy to draw this conclusion. Richardson et al. (2007) also suggest that the flatness and extension of their data to shorter wavelengths implies the near absence of water, since previous theoretical models predicted a spectral trough between $\sim$4 and $\sim$8 μm. However, if there is an outer thermal inversion, as we argue here and in Burrows et al. (2007b) is the case for HD 209458b, a trough is flipped into a peak for the same water abundance. This renders moot the use of the spectral slope at the edge of the IRS spectrum to determine the presence or absence of water. One of our major conclusions, implicit in Figures 4 and 5, is that water is not depleted at all in the atmosphere of HD 209458b.

The recent controversies surrounding such an interpretation occasion the following remarks. One thing to bear in mind concerning the use of these IRS spectra to infer compositions is that they are very low resolution. The use of classical astronomical spectroscopy to identify constituents stems from the ability at much higher resolution to see characteristic features at precise wavelengths and patterns of absorption or emission lines to high accuracy. This allows one to make element and molecule identifications in a narrow wavelength range without a global view across the whole spectrum. However, at the low resolution of the IRS, no individual water features are accessible. There are water features near $\sim$10 μm, but for them to be identified would require a $\lambda/\Delta\lambda$ in excess of $\sim$2000. Otherwise, all one sees is the collective effect of millions of lines and the resulting pseudocontinuum (the band structure). Clearly, when the data are low resolution, a *global* photometric and spectral fit is necessary to address the issue of composition. The signature of water's presence comes from the goodness of the global fit across the entire spectrum from the optical to the mid-IR. The good fit we obtain in Figure 4 leads us to conclude that the IRS, IRAC 4, and MIPS data for HD 209458b are consistent with the presence of water in abundance.

Note that if the T/P profile were entirely flat (but see Fig. 1), whatever the opacity and molecular abundances the emergent spectrum would be a perfect blackbody and would give no hint concerning composition. Transit spectra would then be our only reliable means of determining atmospheric composition (Fortney et al. 2003; Barman 2007; Tinetti et al. 2007; Ehrenreich et al. 2007). However, as we have argued, there is every indication that the T/P profiles of strongly irradiated EGPs are not flat (Fig. 1). As a result, spectral measurements of irradiated EGPs can be used as a diagnostic of both composition and nontrivial thermal profiles.

4.2. *HD 189733b*

Models for HD 189733b at secondary eclipse, with and without an extra upper atmosphere absorber, are portrayed in the top right-hand panel of Figure 4. They include $\kappa_e = 0.0$ cm^2 g^{-1} models with $P_n = 0.1$, 0.3, and 0.5, and one $\kappa_e = 0.04$ cm^2 g^{-1} model with $P_n = 0.3$. The IRAC 4 data at 8 μm from Knutson et al. (2007b) (*brown*), the IRS peak-up point at 16 μm obtained by Deming et al. (2006) (*gray*), and the IRS spectrum between $\sim$7.5 and $\sim$13.5 μm from Grillmair et al. (2007) (*gold*) are superposed on the figure. Although data in the other IRAC channels and at 24 μm have been taken and reduced, they have yet to be published.

As this panel indicates, the IRAC 4 point can be fit by models that include most values of P_n, with a very slight preference for lower values from 0.1 to 0.3. The IRS data are not well calibrated but do evince the slight turndown at the shorter wavelengths characteristic of atmospheres with weak or no stratospheric absorber. This turndown is in contrast with the behavior of the Richardson et al. (2007) IRS data for HD 209458b and reinforces the conclusion that a thermal inversion, if present in HD 189733b, is very slight (see Fig. 1, *top right*). However, the 16 μm point of Deming et al. (2006) is a bit higher than models with $\kappa_e = 0$, whatever the value of P_n. This suggests that there may be some extra heating in the upper atmosphere of HD 189733b, but that it is weaker than in the atmosphere of HD 209458b. The $\kappa_e = 0.04$ cm^2 g^{-1} model shown in the HD 189733b panels of Figures 1 and 4 indicates the possible magnitude of such stratospheric heating, if present. Note that to fit the 16 μm point we require a smaller value of κ_e than used to fit the IRAC channel data for HD 209458b ($\kappa_e = 0.1$ cm^2 g^{-1}). This may not be surprising, since, as Table 1 indicates, the stellar flux at the substellar point of HD 189733b is lower by more than a factor of 2 than the corresponding number for HD 209458b. Perhaps this indicates a systematic trend for the family of strongly irradiated transiting EGPs (see Tables 1 and 3), with planets with the higher values of F_p possessing stratospheres and atmospheres with pronounced inversions.

Be that as it may, we can predict, using the logic presented in § 4.1, that if the IRAC 1 to IRAC 2 ratio turns out to be greater than or close to 1, any thermal inversion in the atmosphere of HD 189733b is either not pronounced or is absent. Under these circumstances, we certainly would then expect the "brightness" temperature at IRAC 1 to be demonstrably higher than that at IRAC 2 (see, e.g., Fig. 2). Conversely, if the IRAC 1 to IRAC 2 ratio is much less than 1 (as for HD 209458b), then a thermal inversion in the atmosphere of HD 189733b would be strongly suggested. The same can be said of the IRAC 4 to IRAC 3 ratio. If the IRAC channel 3 planet-to-star flux ratio is higher than the Knutson et al. (2007b) point at 8 μm, then a stratosphere would be indicated for HD 189733b. Since the irradiation regime of HD 189733b is a bit more benign than that of HD 209458b, and given the contrast in the short-wavelength behavior of the IRS data for each EGP, we hypothesize that HD 189733b does not

boast much of a stratosphere. Note that our HD 189733b models all have water in abundance and that if the unpublished IRAC 1, 2, and 3 data for HD 189733b prove to decrease monotonically with wavelength shortward of IRAC 4, this would be fully consistent with the presence of the water band between ~4 and ~8 μm in absorption.

4.3. TrES-1

Charbonneau et al. (2005) obtained IRAC 2 (~4.5 μm) and IRAC 4 (~8.0 μm) data for TrES-1 and these data were analyzed by Burrows et al. (2005). A major conclusion of that paper was that water is indeed seen in absorption. Our new models, depicted in the bottom left panel of Figure 4 with the two IRAC data points superposed, reinforce this finding. As can be seen in the figure, the models with different values of P_n (here all with $\kappa_e = 0$) cannot easily be distinguished using these two IRAC points. This fact emphasizes the need to obtain more Spitzer photometric data to help better constrain the properties of the atmosphere of TrES-1. However, it is clear from the significant drop in planet/star flux ratio from IRAC 4 to IRAC 2 that the atmosphere of TrES-1 is qualitatively different from that of HD 209458b. In particular, this behavior is a signature of a strong water absorption trough. There are no signatures of a thermal inversion in the atmosphere of TrES-1, or of water in emission, and the old, default models with a monotonic temperature profile (see Fig. 1, *left middle*) are perfectly suitable. Given this, we predict that the IRAC 1 point (when obtained) will be slightly higher than the IRAC 2 point.

4.4. HD 149026b

As is suggested by the relative values of F_p found in Table 1 for HD 209458b, HD 189733b, and TrES-1 and the different thermal profiles inferred for their atmospheres, there appears to be a correlation between the character of a planet's atmosphere and its value of F_p, or a related quantity (UV insolation?). This possibility is intriguing, but not yet explained. In particular, we have yet to identify the extra stratospheric absorber in that subset of close-in EGPs "clearly" manifesting thermal inversions. However, (1) HD 149026b's F_p is almost twice that of HD 209458b, (2) it has one of the hottest atmospheres among those listed in Table 1 (see middle left panel of Fig. 1), and (3) we cannot fit the IRAC 4 data point obtained by Harrington et al. (2007) without a strong temperature inversion. The latter conclusion agrees with that of Fortney et al. (2006), who predicted a mid-infrared flux for HD 149026b near the value actually measured by Harrington et al. (2007) by allowing TiO/VO to reside at low pressures for the hottest atmospheres (Hubeny et al. 2003). The bottom right panel of Figure 4 depicts three models for HD 149026b, one of which has $\kappa_e = 0.64$ cm^2 g^{-1}. This is much larger than the κ_e employed to fit HD 209458b. The stratospheric model shown has $P_n = 0.0$, which minimizes the value of κ_e necessary to fit the lone Harrington et al. (2007) data point, and it is the only model among the three depicted in Figure 4 that does fit. Therefore, the trend in "inversion" strength" with F_p, seen in the sequence TrES-1, HD 189733b, and HD 209458b, continues with HD 149026b. Not only do the EGP atmospheres grow hotter with F_p (a not unexpected result), but the importance of a thermal inversion and a stratosphere in explaining the extant data increases with it as well. Given the current paucity of data for HD 149026b, we urge that HD 149026b be a priority target so as to help discriminate the various models only partially represented on the HD 149026b panel of Figure 4. We predict that the pattern of the four IRAC flux ratios for HD 149026b will mimic that found for HD 209458b, and that its flux ratios from ~10 to ~30 μm will

comfortably exceed those of models without obvious thermal inversions, perhaps by large margins.

5. LIGHT CURVES: COMPARISON WITH DATA

Measuring the infrared planet-star contrast ratio as a function of orbital phase, i.e., the planet's light curve, provides the best constraints on the longitudinal distribution of planetary emissions. In principle, phase-dependent light curves at different wavelengths can be inverted to determine the "brightness" temperature and composition distributions over the surface of the planet, including its night side. Contrast ratios obtained not just at secondary eclipse ($\alpha = 0°$) but also at other phase angles help reveal and quantify zonal winds and establish their role in redistributing stellar energy (i.e., P_n) and matter around the planet. They can help identify transitions at the terminator (Guillot & Showman 2002; Showman & Guillot 2002), shifts in the substellar hot spot (Cooper & Showman 2005; Williams et al. 2006), asymmetries in the thermal distributions (Knutson et al. 2007b), and persistent atmospheric structures. In sum, light-curve measurements probe both atmospheric dynamics and the planet's climate and are the key to the bona fide remote sensing of exoplanets.

Having said this, since full light curves require many more pointings and much more telescope time to obtain, and mostly address the dimmer phases of a planet's orbital traverse, obtaining them is much more difficult than measuring the contrast ratio at secondary eclipse. As a result, to date there are only three published light curves for irradiated EGPs (for υ And b, HD 179949b, and HD 189733b), despite numerous observational forays. All of these are for only one Spitzer wave band each, and none covers a complete orbit. There do exist recent upper limits (e.g., Cowan et al. 2007), but these are not usefully constraining, and we do not address them here.[5]

Below we discuss the three systems for which light curves, however sparse, have been obtained and try to extract physical information by comparison with our light-curve models (eq. [1]). Before we do so, we note the following. Classic light-curve studies are in the optical and measure geometric albedos, phase functions (Sudarsky et al. 2005), and polarizations, i.e., they measure reflected stellar light. Albedos and polarizations are significantly affected by the presence of clouds, and so these traditional optical campaigns focus on reflection by condensates or surfaces. The planet-star flux ratios in the optical range from ~10^{-10} for EGPs at AU distances to ~10^{-5} to 10^{-6} for the close-in EGPs near ~0.05 AU (Table 1). However, in the near- and mid-IR, the planet-star contrasts are around ~10^{-3} (see Figs. 4 and 5). These larger numbers are why Spitzer IR measurements, rather than optical measurements, have assumed center stage in the direct study of EGPs. The light seen is not reflected stellar light, but reprocessed stellar flux, emitted predominantly in the near- and mid-IR (Fig. 3) at the lower temperatures (~1000–2000 K) of the resulting planetary atmospheres. The ratio between the optical and IR components, and thus the relative advantage of IR measurements, is roughly the square of the ratio between the orbital distance and the stellar radius, a number near ~10^2 for most of the planets listed in Table 1.

5.1. υ And b

Harrington et al. (2006) have measured the phase variation at 24 μm of the planet-star contrast for the close-in EGP υ And b (Butler et al. 1997). Since this planet is not transiting, we

---
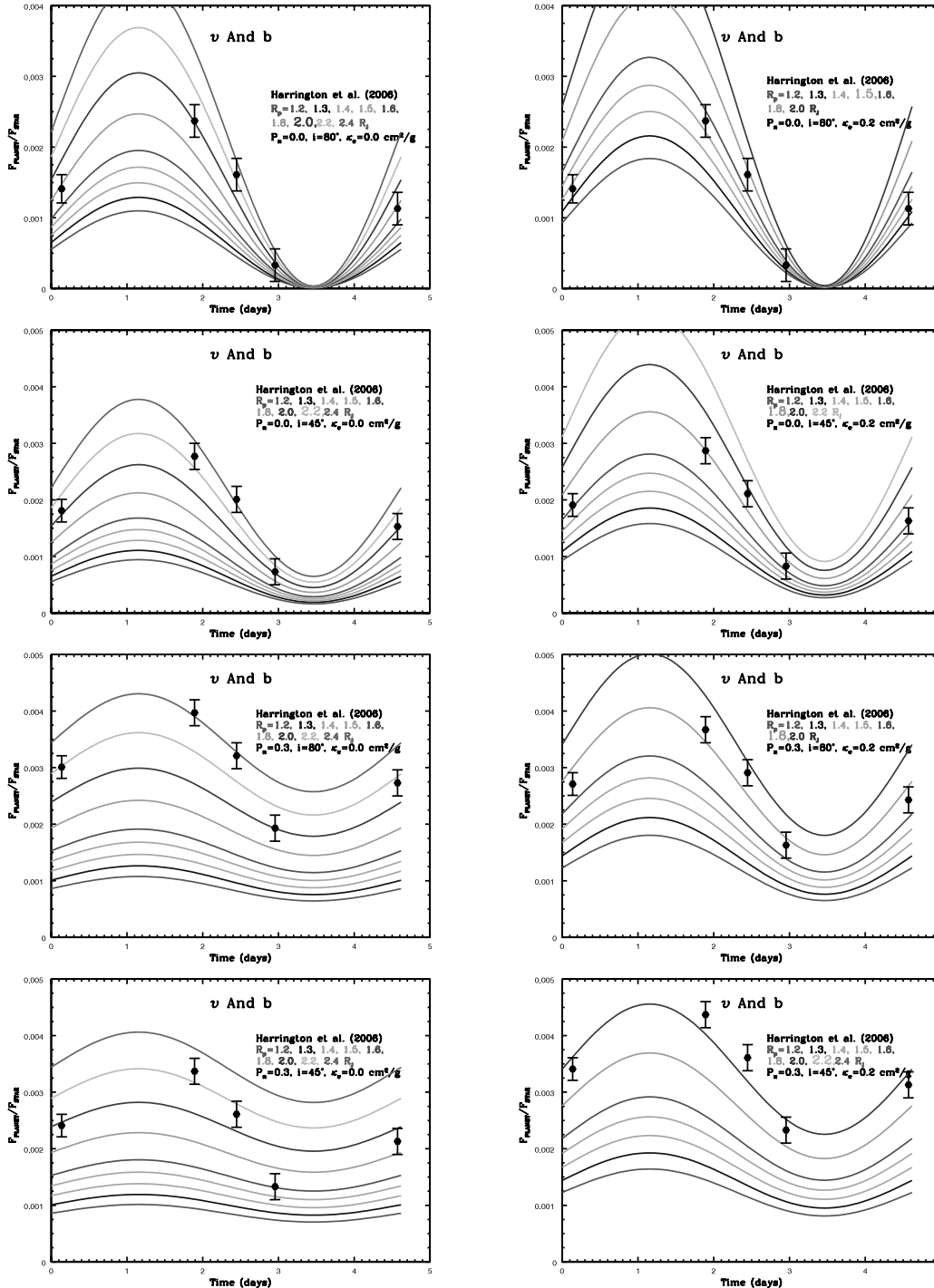
[5] However, a few of these limits are listed in Table 3.

FIG. 6.—Theoretical light curves for the nontransiting EGP υ And b in the MIPS 24 μm band for different inclinations ($i = 45°$ and $80°$), values of P_n (0.0 and 0.3), values of κ_e (0.0 and 0.2 cm^2 g^{-1}), and a range of planetary radii. Superposed are the light-curve measurements of Harrington et al. (2006). Note that Harrington et al. (2006) obtain only relative contrast values, not absolute values. Therefore, the data on each panel are shifted in absolute contrast space, while maintaining the measured relative values. The day/night contrast difference is preserved. In this way, we find the corresponding best fits consistent with the observations, but for different inclinations, etc. Note that the scales for the different panels can be different, although the right panel that faces each left panel has the same scale as that left panel. The left panels depict models without a thermal inversion, while the right panels depict models that have thermal inversions created using $\kappa_e = 0.2$ cm^2 g^{-1}. Together, this set of panels illustrates the dependence on the three most important free parameters: P_n, i, R_p, and κ_e. See text for a discussion. [*See the electronic edition of the Journal for a color version of this figure.*]

know neither M_p nor sin (i), but only the combination M_p sin (i) (=0.69 M_J). Moreover, without a transit we do not have a measurement of R_p. In fact, the models used to fit the five (!) data points obtained by Harrington et al. (2006), which are not anchored by absolute calibration and depend on P_n, κ_e, R_p, and sin (i) (see eq. [1]). In addition, all interpretations hinge on only the two extreme points in the Harrington et al. (2006) data set.

Therefore, we have too many degrees of freedom to allow us to draw strong conclusions concerning planetary and atmospheric parameters and must make do with limits and general correlations.

Figure 6 portrays in eight panels comparisons of theoretical 24 μm phase curves with the υ And b data. The left panels contain models with $\kappa_e = 0$, and the right panels contain models with $\kappa_e = 0.2$ cm^2 g^{-1}. The models in the top four panels have

$P_n = 0.0$, and those in the bottom four panels have $P_n = 0.3$. Inclinations of both $45°$ and $80°$ (near eclipse) are employed. On each panel we provide models with a wide range of planetary radii. Since the data have no absolute calibration, we are free to move the data points up and down, as long as their relative values are maintained, and we have done so in an attempt to provide on each panel the best fit to the overall shape and the day/night difference. The corresponding T/P profiles at $\alpha = 0°$ (day) and $\alpha = 180°$ (night) are displayed in the bottom left panel of Figure 1.

From figures such as Figure 6, we can extract general trends and limits. In their discovery paper the authors noted that the shift of the hot spot away from the substellar point was small. They also remarked on the large difference from peak to trough (~ 0.002). Both observations suggested that there is not much heat redistribution from the day side to the night side and that P_n is small, perhaps near zero. While at this stage this conclusion cannot be refuted, our models suggest that there is a broader range of possible interpretations. Importantly, as we have noted in § 4, the presence of a stratosphere can enhance dayside planetary fluxes in the mid-IR, and certainly near 24 μm, even for modest values of P_n which would otherwise decrease D/N (eq. [1]). υ And b experiences a substellar flux, F_p, of $\sim 1.3 \times 10^9$ ergs cm^{-2} s^{-1}, and this is larger than that impinging on HD 209458b. Therefore, we expect that the atmosphere of υ And b will have a thermal inversion as well, thereby enhancing the mid-IR day/night contrasts even for values of P_n near 0.3.[6] What is more, large values of R_p are becoming commonplace, and we cannot eliminate this possibility for υ And b. A large value of R_p increases the amplitude swing from day to night. Therefore, many parameter combinations can fit these data.

We summarize the lessons of Figure 6 as follows. All else remaining the same, a change of P_n from 0.0 to 0.3 results in an increase in the R_p required of $\sim 0.3–0.5$ R_J. Substituting $\kappa_e = 0.2$ cm^2 g^{-1} for $\kappa_e = 0.0$ decreases the R_p necessary by $\sim 0.4–0.5$ R_J. Replacing models with $i = 45°$ by those with $i = 80°$ decreases the R_p required by $\sim 0.2–0.3$ R_J. Specifically, a (P_n, κ_e, i) = ($0.0, 0, 80°$) model has a required radius of ~ 2.0 R_J (Fig. 6, *top left*), while a (P_n, κ_e, i) = ($0.0, 0.2, 80°$) model has a required radius of ~ 1.5 R_J (Fig. 6, *top right*). And while a (P_n, κ_e, i) = ($0.3, 0, 80°$) model requires an R_p of ~ 2.5 R_J, one with $\kappa_e = 0.2$ cm^2 g^{-1} requires a radius of "only" ~ 1.8 R_J. Clearly, introducing stratospheres into the mix allows P_n to assume a range of nonzero values for which heat redistribution would not be considered small. However, the implied planetary radius would not be small either, although it would still be within the currently measured range.

Some of this degeneracy might be broken with light-curve measurements at many wavelengths and with a more rapid cadence. Furthermore, astrometric measurements of the stellar wobble can provide sin (i) and the planet's mass, eliminating one important ambiguity. *Spitzer* can still be used to provide the former, while the latter is well within reach of ground-based astronomy. Finally, we would be remiss if we did not mention that *JWST* will inaugurate an era of stunning photometric improvement (by a factor of at least $\sim 10^2$) over current IR platforms for the study of the light curves of both transiting and nontransiting EGPs.

5.2. HD 179949b

Cowan et al. (2007) obtained a light curve in IRAC channel 4 (~ 8 μm) of another nontransiting giant planet, HD 179949b

(Santos et al. 2004; Wittenmyer et al. 2007). It has an M_p sin (i) of ~ 0.95 M_J and a value of F_p of $\sim 1.32 \times 10^9$ ergs cm^{-2} s^{-1}. This makes it similar to the υ And system, both in its general properties and in the limitations on what can be uncovered.

The bottom right-hand panel of Fig. 1 displays the day- and nightside T/P profiles of the light-curve models used to model these data. Figure 7 portrays the corresponding eight-panel figure comparing our theoretical models for various combinations of P_n, κ_e, sin (i), and R_p with the eight data points of Cowan et al. (2007). Figure 7 is similar to Figure 6, but the thermal inversion models are for $\kappa_e = 0.08$ cm^2 g^{-1} and the range of model radii are different. The data for HD 179949b are important, but no less ratty than those for υ And b. Nevertheless, the values of R_p required to fit HD 179949b are systematically lower.

We summarize our conclusions from Figure 7 as follows. A change of P_n from 0.0 to 0.3 requires R_p to increase by $\sim 0.1–0.2$ R_J. Replacing $\kappa_e = 0.0$ cm^2 g^{-1} by $\kappa_e = 0.08$ decreases R_p by $\sim 0.2–0.4$ R_J. Substituting models with $i = 45°$ for those with $i = 80°$ decreases R_p by $\sim 0.1–0.2$ R_J. A (P_n, κ_e, i) = ($0.0, 0, 80°$) model that fits the data requires a radius of ~ 1.2 R_J (Fig. 7, *top left*), while a (P_n, κ_e, i) = ($0.0, 0.08, 80°$) model requires a radius of ~ 1.0 R_J (Fig. 7, *top right*). Whereas a (P_n, κ_e, i) = ($0.3, 0, 80°$) model requires an R_p of ~ 1.6 R_J, one with $\kappa_e = 0.08$ cm^2 g^{-1} requires a much smaller radius, ~ 1.1 R_J. These radii are unexceptional, and in general the presence of a stratosphere substantially decreases the values required to fit these data. Therefore, for HD 179949b we can fit the light-curve data with a quite reasonable combination of parameters, although the various degeneracies still need to be broken.

Finally, Figure 7 suggests that the shift between the transit ephemeris and the light-curve phases is not large, so we do not see any obvious advection downstream of the hot spot. This is consistent with the interpretation by Harrington et al. (2007) of the υ And b phase curve (Fig. 6) and may be a feature of EGPs with stratospheres and/or hot upper atmospheres. While very tentative, this suggestion is reinforced by the observation that there is a definite displacement of the hot spot of HD 189733b, which seems to have a cooler upper atmosphere (Fig. 1). However, the perception of meaningful differences in the displacements of hot spots could just as easily be false and be a consequence of having better data for HD 189733b. Moreover, we do not yet have a good model for the origin of such differences and possible correlations with P_n. Clearly, better sampled phase curve data would be very useful.

5.3. HD 189733b

Currently, the only light curve we have for a transiting EGP was obtained in IRAC 4 at ~ 8 μm by Knutson et al. (2007b).[7] Not only do we have HD 189733b's radius (Table 1), but these light-curve data have absolute calibrations. In addition, there is dense coverage over a bit more than half the orbit, from just before secondary eclipse to just after primary transit. Knutson et al. (2007b) derive the longitudinal dependence of the surface brightness and find a hot spot shifted by $16° \pm 6°$ east of the substellar point, while the coolest region is shifted about $30°$ west of the antistellar point. Curiously, both the hot spot and the coolest spot are in the same hemisphere. Nevertheless, this is the first "map" of the surface of an exoplanet (Burrows 2007). The authors also found an indication of a nonzero, but small, eccentricity with $e \cos \omega = 0.0010 \pm 0.0002$, where ω is the longitude of periastron, a transit radius at 8 μm of 1.137 ± 0.006 R_J (slightly smaller than the optical radius), a stellar radius of 0.757 ± 0.003 $R_\odot$, and an inclination of $85.61° \pm 0.04°$.

---

[6] It is possible that sin (i) is small and, therefore, that the gravity and M_p are large. It is also possible that a large gravity can shift the breakpoint between EGP atmospheres with and without inversions. However, we suspect that F_p, more than gravity, is the crucial parameter in determining this bifurcation.

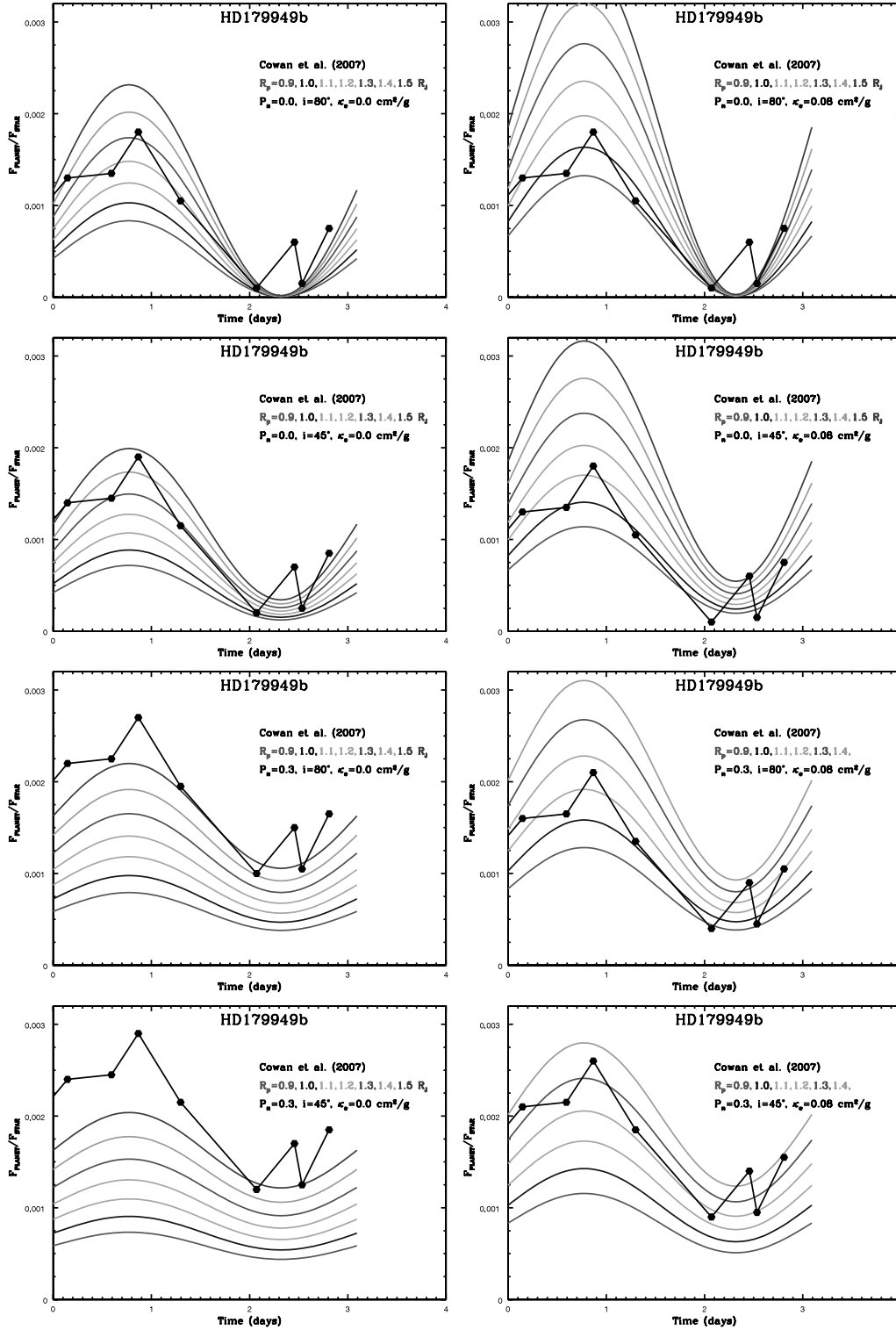[7] However, this is only the first of many anticipated.

FIG. 7.—Same as Fig. 6, but for HD 179949b in the IRAC 4 band for two different inclination angles (45° and 80°), two values of P_n (0.0 and 0.3), a range of planetary radii, and two values of κ_e (0.0 and 0.08 cm^2 g^{-1}). The light-curve data from Cowan et al. (2006) are superposed on each panel. See text for a discussion. [*See the electronic edition of the Journal for a color version of this figure.*]

These data are clearly the best of their kind and we have attempted to fit them with our techniques and equation (1). The results are displayed in Figure 8. The data are plotted as black hexagons, while the models are for various values of P_n. One model (*dashed line*) assumes 10 times solar metallicity. All these models, save one, assume $(P_0, P_1) = (0.1, 1.0)$ bars, not our default pair, but this makes little difference. As indicated in § 4.2,

we can fit the contrast ratio in IRAC 4 at secondary eclipse rather easily, with a slight preference for a small nonzero κ_e. As Figure 8 suggests, a supersolar metallicity might also do the trick, but the metallicity dependence is rather weak. Data in other bandpasses should break the degeneracy.

However, we cannot fit the small day/night difference with any of our models. The data seem to imply a severe degree of heat
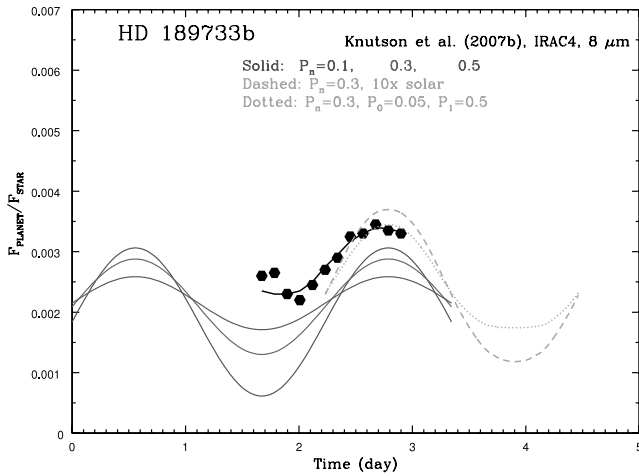
FIG. 8.—Comparison between the light-curve measurements of HD 189733b in the IRAC 4 band (8 μm) performed by Knutson et al. (2007b; *hexagons*) and our theoretical light curves for various values of P_n (0.1, 0.3, 0.5). Most of these models employ values for the redistribution pressure range (P_0 and P_1) of 0.1 and 1.0 bars, but one model (*dotted line*, and $P_n = 0.3$) uses $(P_0, P_1) = (0.05, 0.5)$ bars. See figure legend for model parameters. Also included is a model with 10 times solar metallicity (*dashed line*). All the $P_n = 0.3$ models are in green. See text for a discussion. [*See the electronic edition of the Journal for a color version of this figure.*]

redistribution, one that is still not captured even with our $P_n = 0.5$ model. We note in passing that models with $P_n = 0.5$ do not imply that the day side and night side should look the same, only that the integral fluxes over the entire spectrum should be comparable. Since the day side is irradiated, while the night side emits into the blackness of space, the T/P profiles at $\alpha = 0°$ and $\alpha = 180°$, as the top right-hand panel of Figure 1 indicates, are different. This translates quite naturally into different day-night contrast ratio differences for different wavelengths, even for $P_n = 0.5$.

What we seem to be seeing in the Knutson et al. (2007b) data are atmospheric inhomogeneities, thermal structures (vortices?), on the surface of HD 189733b. That the hot spot and the coolest spot are in the same hemisphere, separated by only ~45°, suggests our symmetric models are inadequate to fit this phase curve. It is of paramount importance that a *full* light curve over all phase angles be taken in a variety of wave bands. Well-sampled data at longer wavelengths would be particularly welcome. Moreover, model phase curves need to be sophisticated enough to incorporate temporal and 3D spatial variations. The light curves and nightside heating and thermal profiles depend centrally on jet streams, winds, and general thermal redistribution. This puts a premium on developing GCMs with reasonable global dynamics coupled to realistic radiative transfer models. Such models do not yet exist for the study of EGPs.

6. DISCUSSION AND CONCLUSIONS

In this paper we have constructed atmosphere and spectral models for all the close-in extrasolar giant planets for which direct-detection data from *Spitzer* have been published (except for the "Neptune" GJ 436b). These models incorporate the effects of external stellar irradiation, detailed atmospheres, heat redistribution, and, for some, a model for stratospheric heating. Comparing the resulting suite of models with the data for these six EGPs, we have derived constraints on their atmospheric properties. We find, as did Burrows et al. (2007b), that many severely irradiated EGPs can have thermal inversions at altitude which translate into qualitative changes in (1) the planet/star contrast ratios at secondary eclipse, (2) their wavelength dependences, and

(3) day-night flux contrasts during a planetary orbit. Absorption features can flip into emission features, planetary fluxes at long wavelengths can be enhanced, and the secondary-eclipse spectra in the near-IR can be altered significantly. What is more, we find a correlation between the importance of such stratospheres and the flux at the substellar point on the planet.

Hubeny et al. (2003) and Burrows et al. (2006) showed that strongly irradiated atmospheres can experience a solution bifurcation to an atmosphere with an inversion for which water spectral features are reversed from troughs (absorption) to peaks (emission). This possibility is supported by the good fits obtained by Burrows et al. (2007b) to the HD 209458b IRAC data (Knutson et al. 2008) and by our models in this paper for the subset of irradiated EGPs for which the presence of stratospheres is suggested (in particular HD 149026b and, perhaps, υ And b). In Hubeny et al. (2003) and Burrows et al. (2006), as well as in the prescient paper by Fortney et al. (2006), the absorber was gasphase TiO/VO, which for hot atmospheres in chemical equilibrium can exist at low pressures at altitude and not just at high temperatures at depth. The upper atmosphere absorber that is producing stratospheres for the higher values of F_p might indeed be TiO/VO, but a "cold-trap" effect can operate to deplete the upper atmosphere of TiO/VO. However, when mass loss is ongoing, as we know to be the case for HD 209458b (Vidal-Madjar et al. 2003, 2004), the atmosphere is constantly being replenished and TiO/VO at some nonzero abundance remains a viable option. Such vigorous mass loss is expected for those planets with the highest values of F_p, and in this paper we have discovered a possible correlation between F_p and the existence of thermal inversions and stratospheres. Hence, the possible massloss/stratosphere connection may make for a compelling scientific narrative.

The tholins, polyacetylenes, or various nonequilibrium compounds discussed in the context of solar-system bodies could also be the necessary upper atmosphere optical absorber. Given the stellar UV and integral-flux regimes experienced by strongly irradiated EGPs, such species might be photolytically produced with sufficient abundance (Burrows et al. 2007b; Marley et al. 2007). However, to study these molecules requires a full nonequilibrium chemical network and we do not attempt this here. Clearly, what the high-altitude absorber actually is, TiO/VO or some other compounds, awaits investigation and is the primary reason we parameterized its opacity with κ_e.[8]

The trend with F_p we have uncovered suggests, however crudely, that those EGPs with values of F_p higher than HD 209458b's (~10^9 ergs cm^{-2} s^{-1}) may well have stratospheres. Table 1 provides the needed numbers. What this table suggests is that TrES-2, TrES-3, TrES-4, HAT-P-2b, HAT-P-4b, HAT-P-5b, HAT-P-6b, OGLE-TR-10b, WASP-1b, WASP-3b, XO-3b, OGLE-TR-56b, OGLE-TR-211b, and OGLE-TR-132b, in addition to HD 149026b, are strong candidates for having stratospheres, with all the consequences implied for their spectra and light curves (§§ 4 and 5). Close-in, but nontransiting EGPs with high values of F_p (such as τ Boo b, to name only one of many) are also likely to have thermal inversions. They too should manifest the spectral discriminants identified in Figures 4 and 5 and the changes in the phase curves discussed in § 5 and suggested by Figures 6 and 7. Note that by including in the above list HAT-P-2b, which has ~10 times the mass of the average close-in EGP, we

---

[8] However, for some of the models in Burrows et al. (2007b) we used equilibrium TiO/VO abundances and the corresponding molecular opacities (Sharp & Burrows 2007). These models reproduced the HD 209458b IRAC data reasonably well.

have not addressed the possible role of gravity in these systematics. Although we suspect gravity is subdominant when compared with F_p, the dependence of upper atmosphere physics and chemistry on gravity should prove worth exploring.

It is unlikely that we will soon obtain spectral data for the OGLE planets. However, it is distinctly possible that EGPs listed in Table 1 with F_p-values slightly lower than HD 208459b's will have "weak" stratospheres, as we speculated may be the case for HD 189733b. This could include XO-2b, HAT-P-1b, WASP-2b, and perhaps XO-1b. We note that F_p for TrES-1 is lower still ($\sim 0.43 \times 10^9$ ergs cm^{-2} s^{-1}) and that this planet shows good evidence for water in absorption and no appreciable stratosphere (§ 4.3 and Burrows et al. 2005). Hence, we have a hint at a breakpoint between EGPs with and without significant stratospheres and thermal inversions.

Despite speculation to the contrary, our models with abundant atmospheric water are fully consistent with all the *Spitzer* data for all the measured EGPs, although at times the water is in emission, not absorption. This conclusion is consistent with the possible identification of water in HD 189733b by Tinetti et al. (2007; although see Ehrenreich et al. 2007) and in HD 209458b by Barman (2007).

We find that the family of close-in EGPs probably boasts a range of values of P_n from ~ 0.1 to ~ 0.4. However, our constraints on this parameter are rather weak, particularly given the possible complicating effects in some EGP atmospheres of a stratospheric absorber. Currently, the presence of such an absorber makes it easier for values of P_n that are not small to explain the data, even for υ And b. However, the magnitude of these effects is hard to pin down with rigor, other than to say they are in evidence—there remains a slight degeneracy between P_n and "κ_e." Without a more first-principles theory concerning the chemistry, spectroscopy, and abundance of this extra absorber at low pressures, and concerning the stellar environment in which it arises, usefully constraining P_n may continue to be difficult. This is the case even if

TiO and VO fit the bill, since their steady-state abundances would still be an issue. Moreover, much better models for redistribution are urgently needed. Lunine & Lorenz (2002) have speculated that planetary atmospheres with jet streams to redistribute dayside heat to the night side adjust their wind dynamics to maximize the rate of entropy generation. Their formalism suggests a value of P_n of ~ 0.2, which is not inconsistent with any of the currently known data on EGP atmospheres.

The direct-detection data we have addressed in this paper are clearly only the first of many anticipated *Spitzer* contrast and light-curve measurements of strongly irradiated EGPs. MOST will continue its campaign, future dedicated space missions will be proposed, and ground-based IR telescopes may have a role. Transiting EGPs are continuing to be discovered at an impressive rate that will not soon abate, providing an expanding catalog for follow-up and characterization. *JWST* is in the wings to revolutionize the field, and will come on line in the middle of the next decade. This paper is meant to provide a broad theoretical context for these initiatives and an interpretive vocabulary with which to address the ongoing study of extrasolar planets in tight orbits around their illuminating stars.

APPENDIX A

AN IMPROVED TREATMENT OF THE REDISTRIBUTION OF STELLAR IRRADIATION FROM THE DAY SIDE TO THE NIGHT SIDE

In this appendix, we describe a slightly more physical version of our previous treatment (Burrows et al. 2006) of the day to night-side redistribution. The total incident stellar flux (expressed as the H-moment) at the planetary surface is

$$H_{\rm ext} = \frac{1}{2}\left(\frac{R_*}{a}\right)^2 \frac{\sigma}{4\pi} T_{\rm eff}^4 = \frac{1}{2}\left(\frac{R_*}{a}\right)^2 H_*, \tag{A1}$$

where R_* is the stellar radius, $T_{\rm eff}$ is the effective temperature of the stellar surface, and a is the planet-star distance. The basic feature of our model is an assumption that out of this total incident stellar flux, a fraction P_n contributes an additional source of energy on the night side, and is removed from the day side. P_n is bounded between 0.0 (no redistribution) and 0.5 ("complete" redistribution) and is conceptually the same as the redistribution parameter employed in Burrows et al. (2006) but is here implemented slightly differently. We introduce

$$H_{\rm irr} \equiv P_n H_{\rm ext} = \frac{P_n}{2}\left(\frac{R_*}{a}\right)^2 H_*. \tag{A2}$$

Formally, we take $P_n > 0$ at the night side (signifying a gain in energy), and $P_n < 0$ at the day side (signifying a sink of energy).

We define a local gain/sink of energy, $D(m)$, such that

$$\int_0^\infty D(m)\,dm = H_{\rm irr}. \tag{A3}$$

We assume that $D(m)$ is nonzero only between column masses m_0 and m_1 (specified through limiting pressures P_0 and P_1, which for our default set of calculations are 0.05 and 0.5 bars, respectively). We have studied the model dependence on the values of P_0 and P_1

around 0.1 to 1.0 bars. The results suggest only a modest effect on the overall spectra at secondary eclipse. However, as the top left panels of Figures 1 and 4 suggest, one can optimally fit the IRAC 2 to IRAC 1 flux ratio for HD 209458b by strategically placing the redistribution band between the corresponding photospheres, and thereby cool the IRAC 1 "$\tau = \frac{2}{3}$" surface relative to the IRAC 2 "$\tau = \frac{2}{3}$" surface. While this did not motivate our default values of P_0 and P_1 (used, one notes, for all objects in this study, not just HD 209458b, and motivated by the desire to redistribute heat near the $\tau_{\text{Ross}} = \frac{2}{3}$ level), the reader should be aware that detailed fits to the secondary eclipse data depend on the choice of P_0 and P_1. Clearly, better models of heat redistribution than we have employed here are called for.

With this caveat in mind, we consider two models for $D(m)$. The first one assumes a constant $D(m)$ between m_0 and m_1:

$$D(m) = \frac{H_{\text{irr}}}{m_1 - m_0}, \qquad \text{(model 1)}. \tag{A4}$$

The second model, model 2, assumes a linearly decreasing $D(m)$ between m_0 and m_1, in such a way that $D(m)$ reaches 0 at $m = m_1$. This is our default model for the calculations of this paper and its functional form is

$$D(m) = \frac{2H_{\text{irr}}}{m_1 - m_0} \frac{m_1 - m}{m_1 - m_0}, \qquad \text{(model 2)}. \tag{A5}$$

Therefore, $D(m)$ is nonnegative on the night side and is nonpositive on the day side.

The first two moments of the transport equation read

$$\frac{dH_\nu}{dm} = \kappa_\nu(J_\nu - B_\nu), \tag{A6}$$

and

$$\frac{dK_\nu}{dm} = \chi_\nu H_\nu, \tag{A7}$$

where κ_ν is the absorption coefficient per gram, χ_ν is the total extinction coefficient (absorption+scattering), and m is the column mass, related to the pressure by the relation $P = mg$, where g is the gravity.

Since we stipulate sinks or sources of energy at certain layers, the usual radiative equilibrium (or radiative+convective) equilibrium does not apply. Instead, it is replaced by the following energy equation, which can be written in two different ways:

1. using the frequency-integrated first moment of the transfer equation,

$$\int_0^\infty \kappa_\nu(J_\nu - B_\nu)\, d\nu = -D(m), \tag{A8}$$

because the energy gained per unit mass, $D(m)$, is balanced by the net radiation loss per unit mass, given by the integral on the left-hand-side of equation (A8);

2. using the equation for the frequency-integrated flux, $H \equiv \int_0^\infty H_\nu\, d\nu$. From eqs. (A6) and (A8), we have

$$\frac{dH}{dm} = -D(m), \tag{A9}$$

which we rewrite as an equation for the integrated H as

$$H(m) = H_{\text{eff}} + \int_m^{m_d} D(m')\, dm', \tag{A10}$$

where m_d is a sufficiently large column mass at which one has $D(m_d) = 0$ (that is, deeper than the region of the sources/sinks), and

$$H_{\text{eff}} \equiv \frac{\sigma}{4\pi} T_{\text{int}}^4 \tag{A11}$$

is the nominal total flux deep in the atmosphere, expressed through an effective temperature, T_{int}.

In view of a simple linear form of $D(m)$, the integral in equation (A10) can be evaluated analytically. We obtain for model 1:

$$
\begin{aligned}
H(m) &= H_{\text{eff}}, & m \geq m_1, \\
H(m) &= H_{\text{eff}} + H_{\text{irr}} \frac{m_1 - m}{m_1 - m_0}, & m_0 \leq m \leq m_1, \\
H(m) &= H_{\text{eff}} + H_{\text{irr}}, & m \leq m_0,
\end{aligned}
\tag{A12}
$$

and for model 2:

$$H(m) = H_{\text{eff}}, \qquad m \geq m_1,$$

$$H(m) = H_{\text{eff}} + H_{\text{irr}} \left(\frac{m_1 - m}{m_1 - m_0} \right)^2, \qquad m_0 \leq m \leq m_1,$$

$$H(m) = H_{\text{eff}} + H_{\text{irr}}, \qquad m \leq m_0. \tag{A13}$$

As suggested by Hubeny & Lanz (1995), it is numerically advantageous to represent the energy balance equation as a linear combination of equations (A8) and (A10), where the H-moment is expressed as $H_\nu = dK_\nu/dm = d(f_\nu J_\nu)/dm$, where f_ν is the Eddington factor. Using the Eddington factor enables us to consider only one radiation moment, J_ν, as an unknown quantity. The Eddington factor is not taken as an unknown; instead it is held fixed in linearization and is recalculated in the formal solution step.

The above equations do not consider convection, so they apply in the radiative zone. In the convection zone, equations (A10), (A12), and (A13) remain unchanged, provided we take

$$H_{\text{eff}} = \frac{\sigma}{4\pi} T_{\text{int}}^4 - \frac{F^{\text{conv}}}{4\pi}, \tag{A14}$$

where F^{conv} is the convective flux. Equation (A8) is modified in the presence of convection to read

$$\int_0^\infty \kappa_\nu (J_\nu - B_\nu)\, d\nu = -D(m) - \frac{1}{4\pi} \frac{dF^{\text{conv}}}{dm}. \tag{A15}$$

COOLTLUSTY solves the energy equation specified through equations (A11)–(A15) numerically and self-consistently with the set of equations of radiative transfer.

However, one can gain deeper physical insight by developing a simplified gray model, in which we can actually derive analytic expressions for the local temperature. More importantly, such a model allows us to understand what values of the limiting pressures for the sink region on the day side and the corresponding optical depths are physically acceptable. We develop these expressions in Appendices B and C below.

APPENDIX B

A SEMIANALYTIC, GRAY MODEL WITH REDISTRIBUTION

In COOLTLUSTY the exact energy balance equation is solved self-consistently with the radiation transport equation. However, it is very useful to develop a simple gray model that allows us to study the conditions under which the structural equations have a solution at all. On the night side, there is always a solution because we are adding energy at certain layers. However, on the day side, we remove energy at certain layers. If we require these layers to be too deep in the optically thick part of the atmosphere, the only way energy can be removed is to create a negative temperature gradient. If, moreover, we require the region with a negative gradient (the region of the energy sink) to continue to depth, we would eventually reach a negative temperature, which is clearly unphysical.

To demonstrate this and to construct an analytic atmosphere model with redistribution, we closely follow the derivation of the analytic model given in Hubeny et al. (2003), generalizing it to account for departures from radiative equilibrium due to the stipulated sources/sinks of energy. We write the frequency-integrated moment equations (A6) and (A7) using the mean opacities

$$\frac{dH}{dm} = \kappa_J J - \kappa_B B \tag{B1}$$

and

$$\frac{dK}{dm} = \chi_H H, \tag{B2}$$

where κ_J, κ_B, and χ_H are the absorption-mean, Planck-mean, and flux-mean opacities, respectively, and J, H, and K are the frequency-integrated moments.

The energy balance equation reads (neglecting convection)

$$\kappa_J J - \kappa_B B = -D(m), \tag{B3}$$

which is just another form of equation (A8).

First, we obtain the solution for the second moment K. We write the second-moment equation as

$$\frac{dK(\tau)}{d\tau} = H(\tau), \tag{B4}$$

where $d\tau \equiv \chi_H dm \approx \chi_{Ross} dm$ is the flux-mean optical depth, which can be approximated as the Rosseland optical depth. In order to integrate the second-moment equation analytically, we introduce the limiting optical depths $\tau_0 \equiv \tau(m_0)$ and $\tau_1 \equiv \tau(m_1)$, and adopt the following approximation for $H(\tau)$:

$$H(\tau) = H_{eff} + H_{irr}\left(\frac{\tau_1 - \tau}{\tau_1 - \tau_0}\right)^n, \qquad \text{for } \tau_0 \le \tau \le \tau_1, \tag{B5}$$

together with the exact expressions $H(\tau) = H_{eff}$ for $\tau \ge \tau_1$ and $H(\tau) = H_{eff} + H_{irr}$ for $\tau \le \tau_0$. Here $n = 1$ for model 1, and $n = 2$ for model 2. This equation is easily solved and yields

$$K(\tau) = K(0) + (H_{eff} + H_{irr})\tau, \qquad \tau \le \tau_0,$$
$$K(\tau) = K(0) + H_{eff}\tau + H_{irr}\left\{\tau_0 + \frac{\tau_1 - \tau_0}{n + 1}\left[1 - \left(\frac{\tau_1 - \tau}{\tau_1 - \tau_0}\right)^{n+1}\right]\right\}, \qquad \tau_0 \le \tau \le \tau_1,$$
$$K(\tau) = K(0) + H_{eff}\tau + H_{irr}\left(\frac{1}{n + 1}\tau_1 + \frac{n}{n + 1}\tau_0\right), \qquad \tau \ge \tau_1. \tag{B6}$$

With the LTE-gray model, this equation is in fact an equation for the local temperature. We invoke the Eddington approximation, $K = J/3$, and use the energy balance equation

$$\kappa_B B = \kappa_J J + D(m), \tag{B7}$$

and the fact that $B = (\sigma/\pi)T^4$ to derive the local temperature. We introduce the following quantities:

$$J(0) = 3K(0) = \alpha J_{ext}, \quad H_{ext} = f_H J_{ext}, \quad H_{irr} = P_n H_{ext}, \text{ and } \quad w \equiv H_{eff}/H_{ext}, \tag{B8}$$

and we write $D(\tau)$ instead of $D(m)$ in equation (B7) as an approximate expression:

$$D(\tau) = \frac{H_{irr}}{\tau_1 - \tau_0}\frac{\bar{\chi}}{\bar{\kappa}_B} \equiv \frac{H_{irr}}{\tau_1 - \tau_0}\epsilon, \tag{B9}$$

where $\bar{\chi}$ and $\bar{\kappa}_B$ are the average values of the flux-mean and the Planck-mean opacities in the interval (τ_0, τ_1). Note that in the strict gray model, $\epsilon = 1$. Note also that the ratio w is given by

$$w = (T_{int}/T_*)^4 2(R_*/a)^{-2}, \tag{B10}$$

so that for the case of strong irradiation, $w \ll 1$. Since here we are interested in deep layers, we use the approximation $\kappa_J = \kappa_B$, (which is, however, not valid at the surface layers). Using the above defined quantities, we can express the integrated Planck function (i.e., temperature) through H_{ext} only and derive

$$B = \left[\beta + w\tau + 3P_n q(\tau) + \frac{\epsilon P_n}{\tau_1 - \tau_0}\right]H_{ext}, \tag{B11}$$

where we denoted $\beta = \alpha/(3f_H)$ (which is a constant of order unity), and

$$q(\tau) \equiv \tau_0 + \frac{1}{n + 1}(\tau_1 - \tau_0)\left[1 - \left(\frac{\tau_1 - \tau}{\tau_1 - \tau_0}\right)^{n+1}\right], \tag{B12}$$

for $\tau_0 \le \tau \le \tau_1$, $q(\tau) = 0$ for $\tau \le \tau_0$, and $q(\tau) = q(\tau_1)$ for $\tau \ge \tau_1$. Notice also that since $B = (\sigma/\pi)T^4$, equation (B11) can be understood as an equation for the local temperature.

APPENDIX C

CONDITION FOR THE EXISTENCE OF THE SOLUTION ON THE DAY SIDE

We now investigate the existence conditions for the solution on the day side. We first make the following approximations: $\alpha = 2$, $f_H = 1/2$; thus, $\beta = 4/3$, $\epsilon = 1$. We assume that $\tau_0 \ll \tau_1$, so we neglect it in the expression for $q(\tau)$. We also introduce the notation $p_n = -P_n$, noting that p_n is a positive quantity. Let us first take model 1, in which $n = 1$. Using all the above approximations, we obtain for the region between τ_0 and τ_1:

$$B(\tau)/H_{ext} = \beta - \frac{p_n}{\tau_1} + w\tau - p_n\tau\left(1 - \frac{\tau}{2\tau_1}\right). \tag{C1}$$

Since τ_1 is typically larger than 1, we neglect the term p_n/τ_1 compared to β. This is not necessary for the formal development, but it simplifies the resulting expressions. The derivative $dB/d\tau = w - p_n(1 - \tau/\tau_1)$; therefore, the local minimum of $B(\tau)$ is at $\tau \equiv \tau_{\min} = \tau_1(1 - w/p_n)$. Since the most interesting case is for strong irradiation where $w \ll 1$, we see that the minimum of B is close to τ_1. The value of $B(\tau)$ at the local minimum is

$$B_{\min} = B(\tau_{\min}) = \beta - \frac{\tau_1 p_n}{2}\left(1 - \frac{w}{p_n}\right)^2. \tag{C2}$$

The condition for the existence of the solution is that $B_{\min} > 0$, and thus

$$\tau_1 < \frac{2\beta}{p_n}\left(1 - \frac{w}{p_n}\right)^2. \tag{C3}$$

Taking the most interesting case of strong irradiation, we can neglect the second factor and write simply

$$\tau_1 < \frac{2\beta}{p_n} \approx \frac{8}{3p_n}. \tag{C4}$$

An analogous analysis for model 2 gives a similar condition,

$$\tau_1 < \frac{4}{p_n}. \tag{C5}$$

For instance, this demonstrates that for $p_n = 0.5$, the case with the maximum energy sink on the day side and the maximum degree of redistribution, the deeper (high-pressure) limit of the sink region must be at optical depths less than 8. Equation (C5) indicates that this limit is larger for smaller p_n (e.g., it is 40 for $p_n = 0.1$). Hence, we have derived consistency conditions for our redistribution algorithm that have physical content and in our choices for P_0 and P_1, we are careful not to exceed this condition. Our default values of P_0 and P_1, 0.05 and 0.5 bars, respectively, translate into an optical depth range of a few times 0.1 to roughly a few, within the consistency constraints for all the P_n-values. Indeed, if we were to exceed the consistency constraints in our atmosphere calculations, they would not converge and the simulations would crash numerically.

APPENDIX D

THE ORIGIN OF THE $f = \frac{2}{3}$ TERM

To derive the proper f factor, we now expand on the formalism of Appendix A. The total energy flux received by a unit area on the planetary surface at angle θ_0 from the substellar point is given by

$$F(\mu_0) = 4\pi\left(\frac{R_*}{a}\right)^2 H_* \mu_0, \tag{D1}$$

where $\mu_0 = \cos\theta_0$ and θ_0 is the angle between the normal to the planetary surface and the direction toward the star. For simplicity, we assume that the angular diameter of the star is small. Consequently, all rays coming from the star are parallel. $H_* = F_*/4\pi$ and F_* is the radiation flux at the surface of the star. The average flux received by the planet is then

$$F_{\mathrm{av}} = \int_0^1 F(\mu_0)\, d\mu_0 = \frac{1}{2}4\pi H_*\left(\frac{R_*}{a}\right)^2, \tag{D2}$$

which explains the origin of the $f = \frac{1}{2}$ Ansatz.

To improve on this, we assume the Eddington approximation, $J = 3K$, and ignore convection, which allows us to write down an analytic solution of equation (B4) for J:

$$J(\tau) = J_0 + 3H\tau, \tag{D3}$$

where $4\pi H$ is the interior planetary flux. To obtain the constant $J_0 = J(0)$, we employ the formal solution of the transfer equation for the specific intensity:

$$I(0, \mu) = \int_0^\infty (\kappa_J/\kappa_B) J(t) e^{-t/\mu}\, dt/\mu, \tag{D4}$$

since the source function, S, is given by $S = B = (\kappa_J/\kappa_B)J$. As shown by Hubeny el. (2003), κ_j/κ_B can differ significantly from unity, but only for low values of the flux-mean optical depth, $\tau \ll 1$. Therefore, we set $\kappa_J/\kappa_B = 1$, and, using equation (D3), we integrate equation (D4) to obtain

$$I(0, \mu) = J_0 + 3H\mu, \tag{D5}$$

which is the well-known Eddington-Barbier relation. The mean intensity on the planetary surface is given by

$$J(0) = \frac{1}{2}\int_0^1 I(0, \ \mu)\,d\mu + \frac{1}{2}\int_{-1}^0 I^{\mathrm{ext}}(\mu)\,d\mu, \tag{D6}$$

where

$$I^{\mathrm{ext}}(\mu) = \delta(-\mu - \mu_0)F(\mu_0)/\pi, \tag{D7}$$

because we have assumed all incident rays from the star are parallel. The expression $\delta(\ )$ is the Dirac δ-function. Therefore,

$$J_0 = J(0) = \frac{1}{2}J_0 + \frac{3}{2}H + \frac{F(\mu_0)}{2\pi}, \tag{D8}$$

and consequently

$$J_0 = 3H + \frac{F(\mu_0)}{\pi}. \tag{D9}$$

The specific intensity is then given by

$$I(\mu, \ \mu_0) = \frac{F(\mu_0)}{\pi} + 3H(\mu + 1), \tag{D10}$$

where we have given the explicit dependence of the emergent specific intensity on μ_0.

For close-in planets, the irradiation flux is much larger than the intrinsic flux, $4\pi H$, so we neglect the second term. The local atmosphere characterized by angle μ_0 exhibits, within the present approximations, an essentially isotropic emergent radiation pattern, independent of the local polar angle μ and dependent only on the angular distance from the substellar point, μ_0. For the total planetary flux close to secondary eclipse received by a observer at a distance D, we have the expression

$$(D/R_p)^2 F_{\mathrm{obs}} = \int_0^1 I(\mu_0, \ \mu_0)\mu_0\,d\mu_0 = \frac{1}{\pi}\int_0^1 F(\mu_0)\mu_0\,d\mu_0 = \frac{4}{3}\left(\frac{R_*}{a}\right)^2 H_*. \tag{D11}$$

For an average atmosphere characterized by the parameter, f, the external flux is given by equation (D2), where we replace $\frac{1}{2}$ by f. We obtain

$$I(\mu, \ \mu_0) = \frac{F(\mu_0)}{\pi} = 4\left(\frac{R_*}{a}\right)^2 H_* f, \tag{D12}$$

and therefore

$$(D/R_p)^2 F_{\mathrm{obs}} = \int_0^1 I(\mu_0, \ \mu_0)\mu_0\,d\mu_0 = 4\left(\frac{R_*}{a}\right)^2 H_* f \int_0^1 \mu_0\,d\mu_0 = \frac{4f}{2}\left(\frac{R_*}{a}\right)^2 H_*. \tag{D13}$$

In order to get agreement between equations (D11) and (D13), we have to set $f = \frac{2}{3}$. This is the origin of our use of this value.

REFERENCES

Alonso, R., et al. 2004, ApJ, 613, L153
Asplund, M., Grevesse, N., & Sauval, A. J. 2006, Nucl. Phys. A, 777, 1
Bakos, G. A., et al. 2006, ApJ, 650, 1160
———. 2007a, ApJ, 656, 552
———. 2007b, ApJ, 670, 826
———. 2007c, ApJ, 671, L173
Ballester, G. E., Sing, D. K., & Herbert, F. 2007, Nature, 445, 511
Barbieri, M., et al. 2007, A&A, submitted
Barman, T. 2007, ApJ, 661, L191
Barman, T. S., Hauschildt, P. H., & Allard, F. 2005, ApJ, 632, 1132
Beaulieu, J. P., Carey, S., Ribas, I., & Tinetti, G. 2008, ApJ, 677, 1343
Bouchy, F., et al. 2004, A&A, 421, L13

Bouchy, F., et al. 2005, A&A, 444, L15
Burke, C. J., et al. 2007, ApJ, 671, 2115
Burrows, A. 2005, Nature, 433, 261
———. 2007, Nature, 447, 155
Burrows, A., Guillot, T., Hubbard, W. B., Marley, M. S., Saumon, D., Lunine, J. I., & Sudarsky, D. 2000, ApJ, 534, L97
Burrows, A., Hubbard, W. B., Lunine, J. I., & Liebert, J. 2001, Rev. Mod. Phys., 73, 719
Burrows, A., Hubeny, I., Budaj, J., & Hubbard, W. B. 2007a, ApJ, 661, 502
Burrows, A., Hubeny, I., Budaj, J., Knutson, H. A., & Charbonneau, D. 2007b, ApJ, 668, L171
Burrows, A., Hubeny, I., & Sudarsky, D. 2005, ApJ, 625, L135

Burrows, A., & Sharp, C. M. 1999, ApJ, 512, 843
Burrows, A., Sudarsky, D., & Hubeny, I. 2003, in AIP Conf. Proc., The Search for Other Worlds, ed. S. Holt & D. Deming (Melville: AIP), 143
———. 2004, ApJ, 609, 407
———. 2006, ApJ, 650, 1140
Butler, R. P., Marcy, G. W., Williams, E., Hauser, H., & Shirts, P. 1997, ApJ, 474, L115
Cameron, A. C., et al. 2007, MNRAS, 375, 951
Charbonneau, D., Brown, T. M., Latham, D. W., & Mayor, M. 2000, ApJ, 529, L45
Charbonneau, D., Brown, T. M., Noyes, R. W., & Gilliland, R. L. 2002, ApJ, 568, 377
Charbonneau, D., Winn, J. N., Everett, M. E., Latham, D. W., Holman, M. J., Esquerdo, G. A., & O'Donovan, F. T. 2007, ApJ, 658, 1322
Charbonneau, D., et al. 2005, ApJ, 626, 523
Cho, J. Y.-K., Menou, K., Hansen, B. M. S., & Seager, S. 2003, ApJ, 587, L117
Cooper, C. S., & Showman, A. P. 2005, ApJ, 629, L45
Cowan, N. B., Agol, E., & Charbonneau, D. 2007, MNRAS, 379, 641
Deming, D., Harrington, J., Laughlin, G., Seager, S., Navarro, S. B., Bowman, W. C., & Horning, K. 2007, ApJ, 667, L199
Deming, D., Harrington, J., Seager, S., & Richardson, L. R. 2006, ApJ, 644, 560
Deming, D., Seager, S., Richardson, L. J., & Harrington, J. 2005, Nature, 434, 740
Demory, B.-O., et al. 2007, A&A, 475, 1125
Ehrenreich, D., Hébrard, Lecavalier des Etangs, A., Sing, D., Désert, J.-M., Bouchy, F., Ferlet, R., & Vidal-Madjar, A. 2007, ApJ, 668, L179
Fortney, J. J., Marley, M. S., Lodders, K., Saumon, D., & Freedman, R. S. 2005, ApJ, 627, L69
Fortney, J. J., Saumon, D., Marley, M. S., Lodders, K., & Freedman, R. S. 2006, ApJ, 642, 495
Fortney, J. J., Sudarsky, D., Hubeny, I., Cooper, C. S., Hubbard, W. B., Burrows, A., & Lunine, J. I. 2003, ApJ, 589, 615
Gillon, M., Pont, F., Moutou, C., Bouchy, F., Courbin, F., Sohy, S., & Magain, P. 2006, A&A, 459, 249
Gillon, M., Triaud, A. H. M. J., Mayor, M., Queloz, D., Udry, S., & North, P. 2007a, A&A, 466, 473
———. 2007b, A&A, 472, L13
Gillon, M., et al. 2007c, A&A, 471, L51
———. 2007d, A&A, submitted (arXiv:0712.2073)
Grillmair, C. J., Charbonneau, D., Burrows, A., Armus, L., Stauffer, J., Meadows, V., Van Cleve, J., & Levine, D. 2007, ApJ, 658, L115
Guillot, T., Santos, N. C., Pont, F., Iro, N., Melo, C., & Ribas, I. 2006, A&A, 453, L21
Guillot, T., & Showman, A. P. 2002, A&A, 385, 156
Harrington, J., Hansen, B., Luszcz, S., Seager, S., Deming, D., Menou, K., Cho, J., & Richardson, L. 2006, Science, 314, 623
Harrington, J., Luszcz, S., Seager, S., Deming, D., & Richardson, L. J. 2007, Nature, 447, 691
Henry, G., Marcy, G. W., Butler, R. P., & Vogt, S. S. 2000, ApJ, 529, L41
Holman, M. J., Winn, J. N., Stanek, K. Z., Torres, G., Sasselov, D. D., Allen, R. L., & Fraser, W. 2007, ApJ, 655, 1103
Holman, M. J., et al. 2006, ApJ, 652, 1715
Hubeny, I. 1988, Comput. Phys. Commun., 52, 103
Hubeny, I., Burrows, A., & Sudarsky, D. 2003, ApJ, 594, 1011
Hubeny, I., & Lanz, T. 1995, ApJ, 439, 875
Johns-Krull, C. M., et al. 2007, BAAS, 210, 96.05
Knutson, H. A., Charbonneau, D., Allen, L. E., Torres, G., Burrows, A., & Megeath, S. T. 2008, ApJ, 673, 526
Knutson, H., Charbonneau, D., Noyes, R. W., Brown, T. M., & Gilliland, R. L. 2007a, ApJ, 655, 564

Knutson, H., et al. 2007b, Nature, 447, 183
Konacki, M., et al. 2004, ApJ, 609, L37
Kovács, G., et al. 2007, ApJ, 670, L41
Kurucz, R. 1994, CD-ROM 19, Atomic Data for Ca, Sc, Ti, V, and Cr (Cambridge: Smithsonian Astrophys. Obs.)
Lunine, J. I., & Lorenz, R. D. 2002, in 33rd Annual Lunar and Planetary Science Conference (Houston: LPI), 1429
Mandushev, G., et al. 2007, ApJ, 667, L195
Marley, M. S., Fortney, J., Seager, S., & Barman, T. 2007, in Protostars and Planets, ed. B. Reipurth, D. Jewitt, & K. Keil (Tucson: Univ. Arizona Press), 733
McCullough, P. R., et al. 2006, ApJ, 648, 1228
Melo, C., et al. 2006, A&A, 460, 251
Menou, K., Cho, J. Y-K., Hansen, B. M. S., & Seager, S. 2003, ApJ, 587, L113
Moutou, C., Pont, F., Bouchy, F., & Mayor, M. 2004, A&A, 424, L31
Noyes, R. W., et al. 2008, ApJ, 673, L79
O'Donovan, F. T., et al. 2006, ApJ, 651, L61
———. 2007, ApJ, 663, L37
Pollacco, D., et al. 2008, MNRAS, 385, 1576
Pont, F., et al. 2007a, A&A, 465, 1069
———. 2007b, preprint (arXiv:0710.5278)
Richardson, L. J., Deming, D., Horning, K., Seager, S., & Harrington, J. 2007, Nature, 445, 892
Richardson, L. J., Deming, D., & Seager, S. 2003, ApJ, 597, 581
Rowe, J. F., et al. 2006, ApJ, 646, 1241
———. 2007, ApJ, submitted (arXiv:0711.4111)
Santos, N. C., Israelian, G., & Mayor, M. 2004, A&A, 415, 1153
Santos, N. C., et al. 2006a, A&A, 450, 825
———. 2006b, A&A, 458, 997
Sato, B., et al. 2005, ApJ, 633, 465
Seager, S., Richardson, L. J., Hansen, B. M. S., Menou, K., Cho, J. Y.-K., & Deming, D. 2005, ApJ, 632, 1122
Sharp, C. M., & Burrows, A. 2007, ApJS, 168, 140
Showman, A. P., & Guillot, T. 2002, A&A, 385, 166
Shporer, A., Tamuz, O., Zucker, S., & Mazeh, T. 2007, MNRAS, 376, 1296
Snellen, I. A., & Covino, E. 2007, MNRAS, 375, 307
Sozzetti, A., Torres, G., Charbonneau, D., Latham, D. W., Holman, M. J., Winn, J. N., Laird, J. B., & O'Donovan, F. T. 2007, ApJ, 664, 1190
Stempels, H. C., Collier-Cameron, A., Hebb, L., Smalley, B., & Frandsen, S. 2007, MNRAS, 379, 773
Sudarsky, D., Burrows, A., Hubeny, I., & Li, A. 2005, ApJ, 627, 520
Sudarsky, D., Burrows, A., & Pinto, P. 2000, ApJ, 538, 885
Swain, M., Bouwman, J., Akeson, R., Lawler, S., & Beichman, C. 2008, ApJ, 674, 482
Tinetti, G., et al. 2007, Nature, 448, 169
Torres, G., et al. 2007, ApJ, 666, L121
Udalski, A., et al. 2007, A&A, submitted (arXiv:0711.3978)
Vaccaro, T., & Van Hamme, W. 2005, Ap&SS, 296, 231
Vidal-Madjar, A., Lecavelier des Etangs, A., Désert, J.-M., Ballester, G. E., Ferlet, R., Hébrand, G., & Mayor, M. 2003, Nature, 422, 143
Vidal-Madjar, A., et al. 2004, ApJ, 604, L69
Werner, M. W., & Fanson, J. L. 1995, Proc. SPIE, 2475, 418
Williams, P. K. G., Charbonneau, D., Cooper, C. S., Showman, A. P., & Fortney, J. J. 2006, ApJ, 649, 1020
Winn, J. N., Holman, M. J., & Fuentes, C. I. 2007a, AJ, 133, 11
Winn, J. N., Holman, M. J., & Roussanova, A. 2007b, ApJ, 657, 1098
Winn, J. N., et al. 2007c, AJ, 134, 1707
Wittenmyer, R. A., Endl, M., & Cochran, W. D. 2007, ApJ, 654, 625